

Electronic Theses and Dissertations, 2004-2019

2018

Tunable Effect of Metal Ions on Polyelectrolyte Mechanics

Angie Diaz
University of Central Florida

 Part of the [Nanoscience and Nanotechnology Commons](#)
Find similar works at: <https://stars.library.ucf.edu/etd>
University of Central Florida Libraries <http://library.ucf.edu>

This Masters Thesis (Open Access) is brought to you for free and open access by STARS. It has been accepted for inclusion in Electronic Theses and Dissertations, 2004-2019 by an authorized administrator of STARS. For more information, please contact STARS@ucf.edu.

STARS Citation

Diaz, Angie, "Tunable Effect of Metal Ions on Polyelectrolyte Mechanics" (2018). *Electronic Theses and Dissertations, 2004-2019*. 5877.
<https://stars.library.ucf.edu/etd/5877>

TUNABLE EFFECT OF METAL IONS ON POLYELECTROLYTE MECHANICS

by

ANGIE M. DIAZ

B.S. University of Central Florida, 2013

A thesis submitted in partial fulfillment of the requirements
for the degree of Master of Science
in the NanoScience Technology Center
in the College of Graduate Studies
at the University of Central Florida
Orlando, Florida

Spring Term
2018

Major Professor: Hyeran Kang

© 2018 Angie M. Diaz

ABSTRACT

Polyelectrolyte based hydrogel fibers can mimic extracellular matrix and have applications such as drug delivery and tissue scaffolding. Metal ions play a critical role in hydrogel fiber stability via electrostatic interactions, but knowledge of how they modulate mechanical properties of individual polyelectrolyte polymers is lacking. In this study, electrospun polyacrylic acid with chitosan is used as a model system to evaluate ferric ion effect on nanofiber mechanics. Using dark field microscopy imaging and persistence length analysis, we demonstrate that ferric ions modulate the bending stiffness of nanofibers. Young's modulus of individual nanofibers is estimated at values of a few kilopascals, suggesting that electrospun nanofibers possibly exist in a hydrated state. Furthermore, Fourier Transform Infrared (FTIR) spectra indicate the effect of ferric ions on polyacrylic acid molecular bonds. Our results suggest that metal ions can regulate single nanofiber stiffness, thereby providing designs to fabricate hydrogels in a tunable fashion.

Keywords: Hydrogel nanofiber, Young's modulus, persistence length, metal ions

ACKNOWLEDGMENTS

There are many people whose efforts and influence have helped shape and strengthen my work into the thesis that follows. Of these I would firstly like to thank Dr. Hyeran Kang, my thesis chair and mentor. Her wisdom, guidance, and limitless patience allowed me to flourish as a scientist in ways I had not thought possible until now. I would also like to thank Dr. Lei Zhai, one of my committee members and constructive mentor from beginning to end. The third member of my committee, Dr. Laurene Tetard as well. Her efforts and support allowed this project to branch in directions we could not without her and her students' hard work.

This project relied on several other brilliant minds, including Xiaoyan Lu and Zeyang Zhang, who have stayed dedicated throughout. Also, fellow research students Briana Lee and James Heidings in support of several aspects of analysis and characterization. And of course, I would like to express my gratitude to my lab members for their encouragement and support throughout.

Additionally, this study was supported by the National Science Foundation and NASA's 2017 FSGC Dissertation/Thesis Improvement Fellowship. I am quite grateful to these organizations, as well as the Nanoscience Technology Center and the Materials Characterization Facility at the University of Central Florida.

To my siblings and friends—thank you for being there without fail. To my partner Aaron Logsdon, for being supportive and caring on days being a scientist wasn't as rosy. And last but certainly not least to my parents, Martin and Leticia Diaz, who both nurtured and encouraged the curiosity and resilience to follow through.

TABLE OF CONTENTS

ABSTRACT.....	iii
ACKNOWLEDGMENTS	iv
TABLE OF CONTENTS.....	v
LIST OF FIGURES	vii
LIST OF TABLES.....	ix
LIST OF ACRONYMS (or) ABBREVIATIONS	x
CHAPTER ONE: INTRODUCTION.....	1
1.1 Polyelectrolyte hydrogels.....	1
1.1.1 Characteristics of polyelectrolyte hydrogels.....	1
1.1.2 Nanofiber fabrication and characterization.....	3
1.2 Polyelectrolyte nanofiber mechanics	5
1.2.1 Metal ion mediated crosslinking of PAA and CS.....	6
1.2.2. Mechanical properties of PAA and CS hydrogels.	7
1.3 Hypothesis.....	9
CHAPTER TWO: MATERIALS AND METHODS	13
2.1. Nanofiber synthesis by electrospinning	13
2.1.1. Variables Affecting Nanofiber Characteristics.....	13
2.1.2. Fabrication parameters for PAA:CS nanofibers.	16
2.1.3. Conductivity of pre-electrospun solutions.....	17
2.2. Scanning electron microscopy	17
2.3. Infrared Spectroscopy	18

2.3.1. Fourier Transform Infrared Spectroscopy.	18
2.3.2. Atomic Force Microscopy-Infrared Spectroscopy.....	18
2.4. Nanofiber bending mechanics analysis.....	20
2.4.1 Confocal microscopy imaging and persistence length analysis.....	20
2.4.2 Beam theory for nanofiber bending mechanics and Young’s modulus estimation.	21
CHAPTER THREE: RESULTS	29
3.1. Ferric ions modulate the mechanical properties and average length of polyacrylic acid nanofibers.....	29
3.2. Chitosan helps ferric ions modulate the mechanical properties of PAA nanofibers. ..	31
3.3. Electrospun PAA:CS nanofiber Young’s modulus is affected by ferric metal ion.	32
3.4. Characterization sheds light on how ferric metal ions affect individual PAA:CS nanofiber structure.	33
CHAPTER FOUR: DISCUSSION	50
CHAPTER FIVE: CONCLUSION.....	57
REFERENCES	59

LIST OF FIGURES

Figure 1. Reversible swelling of pH dependent PAA hydrogel.....	10
Figure 2. Application of nanofibers in varying industries.	11
Figure 3. Ferric binding modes to carboxylate groups of PAA. Mode of binding depends on environmental influence, but overall ferric metal ions have strong ionic interactions with the polymer.	12
Figure 4. Electrospinning instrumentation setup.	24
Figure 5. NanoIR setup schematic.	25
Figure 6. Measurement of bending stiffness in nanofibers relies on correlation analysis between chosen endpoints.....	26
Figure 7. Bending beam theory application for nanofiber Young's modulus measurement..	27
Figure 8. Representative images of PAA:CS nanofiber SEM	28
Figure 9. Representative dark field confocal microscopy images of electrospun PAA:CS nanofibers at varying ferric metal ion concentrations (0%, 0.04%, 0.07%,0.10%, 0.25%, 0.50%, 1.00%, 2.00%).....	39
Figure 10. The cosine correlation functions are plotted against PAA:CS nanofiber segment length at varying ferric ion concentrations.	40
Figure 11. Electrostatic interaction schematic of PAA with CS and ferric metal ions.....	41
Figure 12. Ferric metal ions influence nanofiber length in a nonlinear manner.	42
Figure 13. Ferric ion modulation of bending stiffness in PAA:CS nanofibers is determined by persistence length analysis.....	43

Figure 14. Comparison analysis of length of nanofibers electrospun with and without chitosan at initial concentrations 0%, 0.04%, 0.07%, and 0.10% of ferric metal ions.	44
Figure 15. Comparison analysis of nanofiber bending stiffness of nanofibers electrospun with and without chitosan at concentrations 0%, 0.04%, 0.07%, and 0.10% of ferric metal ions in box plots.....	45
Figure 16. Nanofiber Fourier Transform Infrared (FTIR) spectra (A) at varying ferric concentrations and (B-E) peak deconvolutions at a range of 1530-1810 cm^{-1}	46
Figure 17. AFM-IR studies of nanofibers at 0.04%, 0.10%, 1.00%, as well as control nanofibers (PAA only).....	47
Figure 18. Conductivity of PAA:CS nanofiber and pre-fabrication component solutions....	48

LIST OF TABLES

Table 1. Application of SEM diameter measurements as well as persistence length (using *Persistence* and *Origin* software) in calculations to give estimations for Young's modulus. 49

LIST OF ACRONYMS (or) ABBREVIATIONS

AFM	Atomic Force Microscopy
AFM-IR	Atomic Force Microscopy-Infrared Spectroscopy
CS	Chitosan
<i>E</i>	Young's modulus
ECM	Extracellular Matrix
Fe ³⁺	Ferric metal ions
FTIR	Fourier Transform Infrared Spectroscopy
GPa	Gigapascals
HCl	Hydrochloric Acid
κ	Flexural rigidity
kPa	Kilopascals
L _p	Bending stiffness
MPa	Megapascals
NanoIR	Nano-infrared
PAA	Polyacrylic Acid
PAA:CS	Polyacrylic acid & chitosan nanofibers
PAA:CS:Fe ³⁺	Polyacrylic acid, chitosan, and ferric metal ion nanofibers
PEC	Polyelectrolyte Complex
SEM	Scanning Electron Microscopy
TEM	Transmission Electron Microscopy

CHAPTER ONE: INTRODUCTION

Polyelectrolyte nanofiber hydrogels demonstrate unique properties that make them exceptional for use in biomedical applications. The chapter that follows aims to inform the reader on background information on polyelectrolyte complexes, including nanofiber metal ion interactions, mechanics, their further creation into hydrogels, and biomedical applications. This thesis' central theme is to understand the characteristics of individual nanofiber mechanics, as well as how their complex interaction with metal ions affect these polyelectrolyte structures.

1.1 Polyelectrolyte hydrogels

Hydrogels are made of hydrophilic polymers able to retain water and swell to many times their size without losing their structured, 3-dimensional networks (Hoffman, 2012). The polymer chains can be synthetic or natural and provide functional groups for solutions to interact with while offering further functionalization of the hydrogel. Materials utilized can be biodegradable and biocompatible while taking advantage of a high surface to volume ratio for maximum interactions with less material requirement of a similar product at a larger scale. Because of their molecular bond interactions, it is possible to make hydrogels reversible in nature by alternating between collapsed or swollen states in reaction to environmental changes such as pH, temperature, electricity, or ionic strength (Wei et al., 2013; Zhong et al., 2015). To reinforce the bonds necessary for flexibility in fluctuating environments, crosslinking is applied chemically or physically (Ahmed, 2015; Maitra & Shukla, 2014).

1.1.1 Characteristics of polyelectrolyte hydrogels. Polyelectrolyte hydrogels are created when two types of polymers of opposite charge are used. Their main form of crosslinking is physical in nature which relies mainly on electrostatic interactions but can also include hydrogen

or van der Waals types of bond forming (Omidian & Park, 2010). Physical bonds are reversible, allowing for unique properties without sacrificing other characteristics afforded to hydrogels due to their inherent none-permanent linking. Chemical bonds, such as covalent or are more permanent and therefore limit hydrogel swelling, as well as requiring more complex procedures for fabrication. Hydrogen and van der Waals bonding could require more complex procedures or limit flexibility of mechanical properties because of their weak attractions not being able to withstand fluctuations or more extreme changes of their environment (Y. Wang et al., 2017; Zhu,, 2015). Because electrostatic interactions of PECs are not permanent, they allow for the hydrogel ability to self-heal. Though the bonds can be severed, the newly open sites can interact with other open bonds and recreate electrostatic links to “heal” the gel in mimicry of healing tissues, an important characteristic of living organisms. Unfortunately, this does come with a sacrifice in mechanical strength that leaves the hydrogels unable to function in strenuous environments such as those seen in living organisms (Haraguchi et al., 2011). Overcoming this leads to creation of a hydrogel capable of sustaining itself for much longer without outside influence and has been done on several occasions through different forms of crosslinking or fabrication including layer-by-layer additions (Lichter et al., 2008), free radical polymerization (Y. Wang et al., 2017), and electrospinning (Desai et al., 2008).

Another aspect of living tissue biology hydrogels can mimic is the extracellular matrix. It was believed that the physical environment in which cells are cultured is not of major importance for studies of live cells so long as the proper nutrients are present, but recent research has shown that the dimensions of the environment a cell is in is just as important as other aspects required for successful culturing (Tibbitt & Anseth, 2009; J. H. C. Wang & Thampatty, 2006). Growing certain

cell lines on flat 2D structures create cells that do not function as they would in their natural environment, leading to erroneous growth through failure to exhibit signaling or proliferation seen in vivo. Hydrogels offer biocompatibility through select polymers for fabrication and mimicry of the highly porous network in the structure of their nanofibers. They have tunable stimuli response that could also be selected for through the right polymer blend and mechanical strength for sturdy scaffolds applied to cell growth when in medium, making them optimal replacements for ECM in biomedical applications to avoid adverse reactions other materials might create (Geckil et al., 2010).

The main factor on which all other characteristics of hydrogels rely on is their ability to swell to many times their weight without completely losing their 3D system of polymers. Components that make up the hydrogel rely on their functional groups for interaction with their environment, leading to a pH and osmotic migration of ionic molecules both into and out of the network in response to changes in stimuli (**Figure 1**). To reach swelling equilibrium, the force of solvent entering the hydrogel must balance with the elastic force of the polymer chains that brace against it. The electrostatic interactions along the chains of polymers give the hydrogel flexibility to break and recreate links without loss of overall structure and are the main driving force for swelling because of their electrostatic repulsion between polymer groups of similar charge. The charge density afforded by the polymer chain functional groups therefore become the main effectors of swelling with higher density offering optimized swelling abilities (Ostroha et al., 2004).

1.1.2 Nanofiber fabrication and characterization. Though hydrogels can be fabricated as one whole material, fabrication of nanofiber mats that swell to become hydrogels offer a less complex method of formation with their own tunability through individual nanofiber fabrication

methods. The process of electrospinning provides a simple method of production at lower cost (Malhotra et al., 2016) but comes with a plethora of its own tunable parameters for nanofiber synthesis. Most of them fall under three categories: the electrospinning apparatus, characteristics of the polymers used, and the influence of the environment in which the nanofibers are electrospun (Angamma & Jayaram, 2016).

Many of the stimuli that determine nanofiber diameter, mechanical strength, and crosslinking abilities have been well studied (Angamma & Jayaram, 2016; Camposeo et al., 2013; D. Li & Xia, 2004) with focus on interplay between the changes of apparatus and response of the different polymer solutions. Characterization of resulting nanofibers has been done mostly as a system (a mat) for mechanical properties, though there have been some studies concentrating more on the individual nanofiber traits. Most measurements of single nanofibers in study have relied on application of atomic force microscopy (AFM), scanning electron microscopy (SEM), or a combination of more than one method of characterization that calls for more complicated, customized processes (Y. Li & Wan, 2017; E. P. S. Tan & Lim, 2004). Unfortunately, this does not allow for a wide sample range but does give insight into nanofiber structure, mechanical properties, and morphology. By optimizing the characteristics of the nanofibers, the hydrogel system limitations change. Nonetheless, across all studies the main goal is to create dependable measures for uniform, un-beaded, mechanically sound nanofibers for optimized hydrogel applications.

Polyelectrolyte nanofiber hydrogels have applications that span across many different industries (**Figure 2**). They have been researched as filtration systems, delivery vehicles, and sensory systems. Arguably, the biomedical field has seen the most growth in hydrogel research

due to the unique abilities allowed through bottom-up approach of fabrication starting at the nano-scale and taking advantage of the high surface to volume ratio. The functional groups of polymers chosen for fabrication can be utilized to create versatile, reversible hydrogels with drug delivery capabilities. The delivery systems take advantage of the characteristic responses of the nanofibers to the environmental changes such as temperature, pH, or light to ensure the hydrogels have a controlled, reproducible reaction (Qiu & Park, 2001). Their reversible nature and self-healing abilities also allow them to be good mimics of tissue for tissue scaffolding, encouraging studies into organ and bone production that could be customized to the patient based on their own cell culturing (Francis Michael et al., 2016). Because of this, tunability of their ECM mimicking mechanical properties has become a focus. Based on different stages of cell proliferation, the hydrogels could be made more porous, swollen into more elastic gels, or encouraged to raise crosslinking for stiffer scaffolds to successfully see the cells to maturity through their varied requirements (Engler et al., 2006; Smyth et al., 2017; Stachowiak et al., 2005). Another application, wound delivery, also takes advantage of these same characteristic abilities but is optimized through the polymers chosen. For instance, chitosan is known to be a biodegradable, non-toxic material with antibacterial properties (Takei et al., 2012). When used in wound dressing hydrogels, not only do they bring the polymer characteristics as an advantage, they also can be tuned to become drug delivery vehicles and are antibacterial in nature (Y. Wang et al., 2017).

1.2 Polyelectrolyte nanofiber mechanics

The influence of nanofiber mechanics on cellular response is crucial to the success of hydrogel control over the desired mechanisms of healing in biomedical applications. As such, characterization of nanofiber features is key in the understanding of their effect for tunability.

Fabrication methods, polymer type, and the crosslinking sort therefore can lead to creation of nanofibers ranging widely in their characteristics. For this study, polyacrylic acid and chitosan were chosen as the main polymer components. Though this system has been studied, characterization of mechanical properties affected by the addition of ferric metal ions still requires further quantitative attention.

1.2.1 Metal ion mediated crosslinking of PAA and CS. Polyacrylic acid is a polymer made up of carboxyl functional groups atop a hydrocarbon backbone, functioning as the main creators of the net negative charge (Chen et al., 2006; L. Li & Hsieh, 2005). These form ionic crosslinks with chitosan's positively charged amine groups in nanofiber fabrication for improved stability in fluctuating pH environments (Chavasit et al., 1988). Nonetheless, they still lack stability and mechanical strength. The resulting hydrogels have instability at higher salt concentrations and greater variance of pH due to the breaking of electrostatic bonds in the hydrogel that take away any reversibility of the nanofiber complex. Furthermore, they have been shown to be soluble in water and are hard to create at pH values in the acidic range (under 3) due to the protonation of chitosan and polyacrylic acid functional groups (Chavasit et al., 1988; Penchev et al., 2008; H. Wang et al., 1997). Care in approach of method of creation does allow for complexation of the nanofibers, but the further stability of the system requires further fortification.

Adding metal ions to polyelectrolyte polymer nanofibers stabilizes the system in varying environments through raising of crosslink density and migration of metal ions for self-healing abilities (Calvo-Marzal et al., 2011; Malhotra et al., 2016; Wei et al., 2013). The metal ions interact mainly with functional groups of polyacrylic acid but also increase swelling abilities due to the density of ionic areas on the nanofibers, which become points of contact for water molecules when

swelling into a hydrogel. The effect of several types of metal ions have been tested on different types of polyelectrolyte complexes with varying degrees of success (Guibal, 2004; Malhotra et al., 2016; Su et al., 2011). Ferric metal ions bound to PAA:CS nanofibers have been shown to create clusters that interact via bidentate bridging with carboxyl groups of PAA as opposed to monodentate bridging or bidentate chelating (**Figure 3**) (Baigorri et al., 2007; Yokoi et al., 1993). Therefore, two molecules of ferric interact with two separate oxygen groups of a single carbon of the carboxyl groups on PAA. This can vary depending on environmental influences or multivalence of the metal ion as well, leading to a 1:1 ratio of carboxyl group to metal ion (monodentate), or formation of bidentate chelation “rings” by sharing one ferric per two oxygen groups of the same carboxyl carbons. Determination of shifting between bridging types can be seen through peak deconvolution studies of Fourier Transform Infrared (FTIR) spectra, in which the numerical difference between PAA carboxylate functional group symmetric and asymmetric bond vibrational infrared peaks are compared to those of PAA:CS with the metal ions. Whether the difference in peaks of the salt (PAA:CS:Fe³⁺) is smaller or bigger than that of carboxylate groups of PAA:CS is characteristic of the type of bonding the metal ions do with the functional group of the polyelectrolytes, as seen in our results in chapter 3.

1.2.2. Mechanical properties of PAA and CS hydrogels. Mechanical properties studied for PAA:CS complexes have focused mainly on the hydrogel as a bulk material with varied preparation methods. One-pot free radical polymerization was studied by Zhong et al., relying on polyacrylic acid, ferric metal ions, and a Bis crosslinker to synthesize hydrogels reliant on ionic and minor covalent links for their strength (Zhong et al., 2016). Difficulty of direct comparison between different studies found in the literature is present in that not all use the same method of characterization calculations or final measurements. Zhong et al.’s study for example, reveals a

stress change in the hydrogels in a 0-1.2 megapascal (MPa) range for varying ferric concentrations, while a study done by Nam et al. showed PAA:CS in varying ratios cast and dried as membranes with measurements of tensile strength ranging from 1-16 MPa (Nam & Lee, 1997). Gulyuz et al. focused on polyacrylic acid hydrogels fabricated through micellar copolymerization with cetyltrimethylammonium (Gulyuz & Okay, 2014). Their results showed Young's modulus both in water (183-605 kPa) and pre-swelling (8-30 kPa) and included fracture stress and stress at break in their analysis. Other work done by Calvo-Marzal et al. used free radical polymerization to create sol-gel transitioning hydrogels with PAA and ferric metal ions (Calvo-Marzal et al., 2011) reliant on voltage for redox-oxidation reactions controlling characteristics and leading to a range of Young's modulus 0.5-2.1 MPa. The development of these various studies demonstrates the importance of the strength of crosslinks within the complexes presented but have not focused on a single method of characterization for rheology. Further study into the electrospinning method with nanofiber mechanics pre-hydrogel swelling therefore, has been lacking.

Nanofiber mechanical studies have been done on a variety of complexes but can be tedious in that they require more intricate and sometimes customized methodology. Isolation of single nanofibers and manipulation to be able to test mechanical characteristics can be difficult and only offer a small sample size outside of 3D mat fabrication which is done through continuous electrospinning until several layers of fibers are stacked on each other. Instrumentation has included nano-indentation through atomic force microscopy, in which the cantilever is used in contact mode to apply a controlled load on the nanofiber to study deformation based on the elastic properties of the nanofiber (Camposeo et al., 2013). More recently, nanotensile testers have been

developed as well in an attempt to study nanofiber mechanics with more standard control through a commercially available method (Y. Li & Wan, 2017).

Beam bending theory is applied to the nanofibers under these methods, assuming them to be prismatic elastic beams with pure bending other than at the substrate-adhered ends (E. P. S. Tan & Lim, 2004). Nanofibers diameter is known to have correlation with its' resulting Young's modulus, in which higher diameter leads to lower Young's modulus (Arinstein & Zussman, 2011; Camposeo et al., 2013). This results in inaccuracy if the measurements are done in very small sample sizes along non-uniform nanofibers. Why this correlation occurs has not been fully understood, though theories range from surface tension influence to supramolecular structures within the individual nanofiber (Arinstein et al., 2007; Jian-Gang Guo and Ya-Pu, 2007). The structure of individual nanofibers has been recognized as important in guidance of characteristics displayed in dry and hydrated states but requires further study for optimization. Application of metal ions has shown a positive influence on nanofiber mechanics, though quantification of effects still requires further study for tunable hydrogels.

1.3 Hypothesis

Ferric metal ions have been shown to influence the PAA mechanical properties through crosslinking effects. However, how the metal ions affect *individual nanofibers* mechanics such as bending stiffness and Young's modulus, have not been shown. We hypothesize that ferric metal ions modulate mechanical properties of nanofibers. To test our hypothesis, an electrospun polyacrylic acid nanofiber with chitosan is used as a model system in evaluation of ferric ion effects on nanofiber mechanics and structure through biophysical studies, structural investigation, and application of beam bending theory.

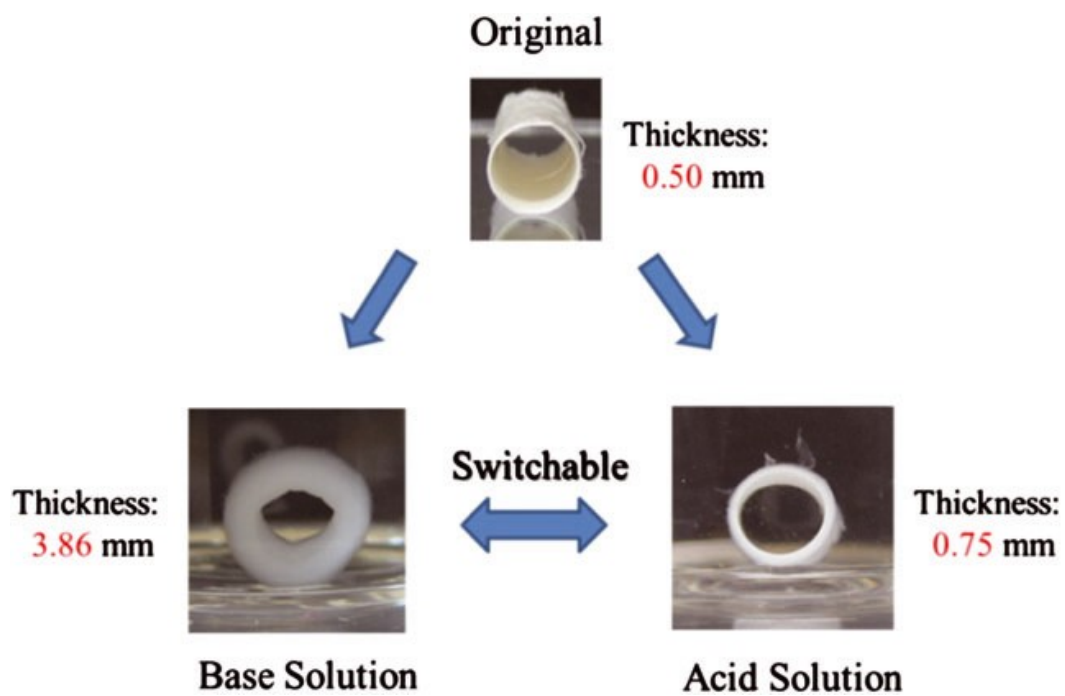


Figure 1. Reversible swelling of pH dependent PAA hydrogel. Cation exchange was used to change the characteristics of the nanofiber tubes without losing their structural integrity. Image reference from: (Meng et al., 2015).

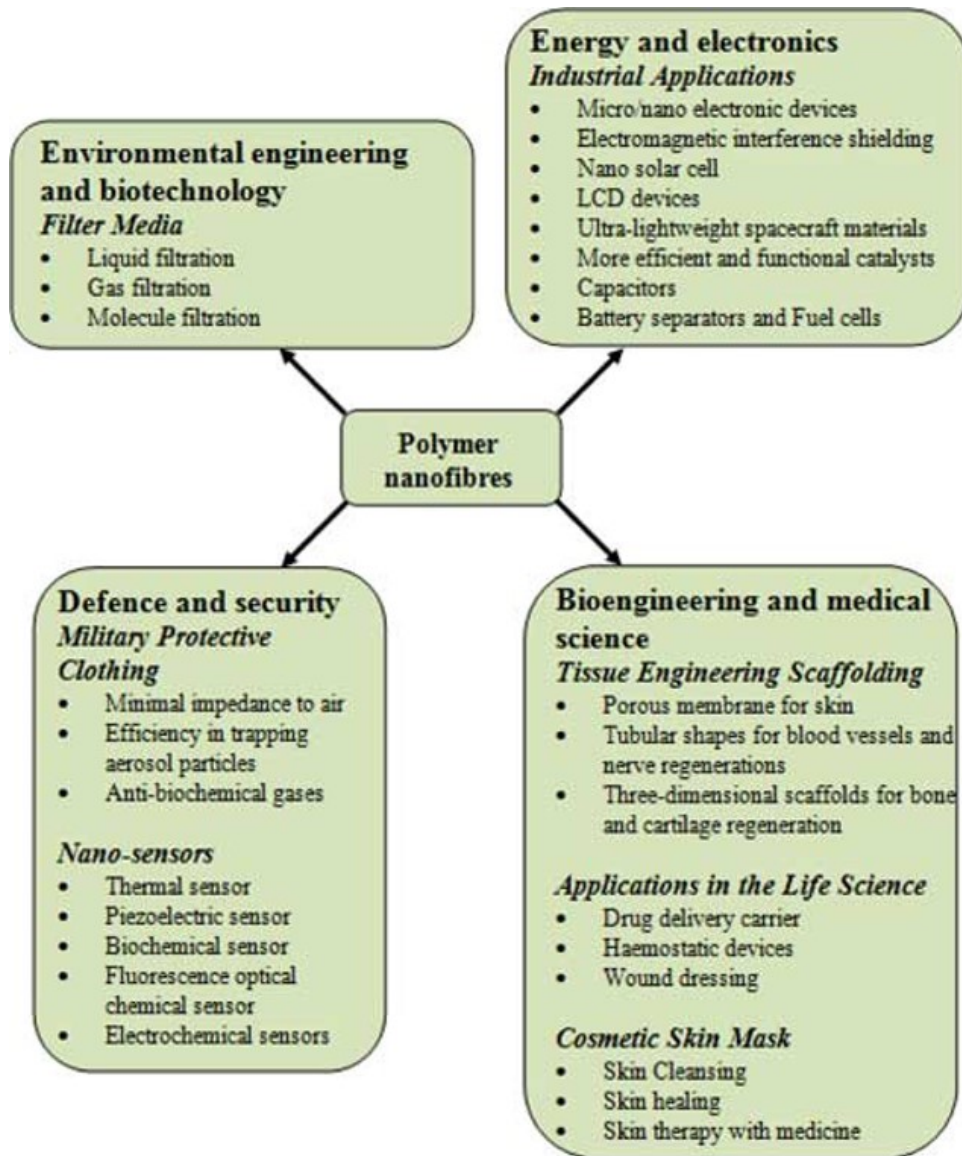


Figure 2. Application of nanofibers in varying industries. Image reference from: (Angamma & Jayaram, 2016).

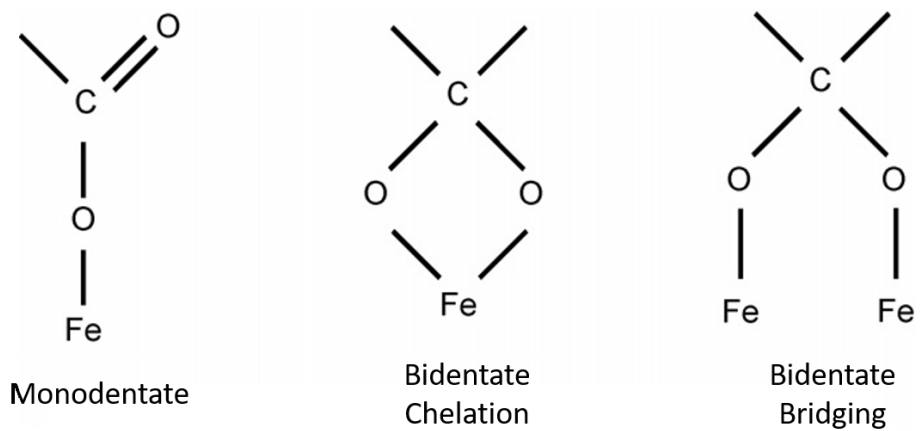


Figure 3. Ferric binding modes to carboxylate groups of PAA. Mode of binding depends on environmental influence, but overall ferric metal ions have strong ionic interactions with the polymer. Image reference from: (Baigorri et al., 2007).

CHAPTER TWO: MATERIALS AND METHODS

2.1. Nanofiber synthesis by electrospinning.

Electrospinning is the process in which nanofibers are formed via electrostatic interactions of the mixture and interaction with voltage applied to that solution. This type of fabrication has great versatility in application and is one of the simplest methods of nanofiber synthesis without losing their vast range of scalability or high production volume abilities (Reneker & Yarin, 2008). The solution is placed in a syringe which is attached to a metal needle while a pump device controls flow rate at which the solution is pushed out. Because the spinneret has an induced positive charge, the fluid is subjected to this as well as electrostatic repulsion of its own ions. Fluid surface tension tends to prefer spherical shapes but attachment of a needle with induced voltage breaks past the surface tension using Coulomb repulsion (D. Li & Xia, 2004). This forces the fluid into a jet-like shape that is pulled towards a collector (with an induced negative charge) down an electrical gradient. Collectors are placed at a calculated distance from the end of the needle so as the nanofiber is produced, all solvent used in the solution evaporates, leaving dry-state nanofibers (**Figure 4**) (D. Li & Xia, 2004). The determination of distance is done through study of the solution being used, solvent added, and testing to see how changes in distance between the spinneret and collector change the morphology (changes in thickness, beading, fiber uniformity). Different solutions have their own optimized parameters which play a major role in the morphology of individual nanofibers, as seen in the following section. The electrospinning parameters used in this study for polyacrylic acid nanofibers with chitosan are shown in section 2.1.2.

2.1.1. Variables Affecting Nanofiber Characteristics. Electrospinning has several parameters that have been studied to optimize nanofiber formation. Instrumentation parameters

include changes in applied voltage, distance between electrodes, and flow rate while solution conductivity, solvent choice, and polymer viscosity impact nanofiber fabrication from the component aspects (Angamma & Jayaram, 2016; Haider et al., 2015; L. Li & Hsieh, 2005; Reneker & Yarin, 2008). The interplay of all parts of the system could make the difference between nanofiber or nanoribbon formation, or whether a solution clumps to create beads, leading instead to electrospaying.

Critical voltage creates nanofibers without formation of beads, and is unique to the nanofiber solution based on the polymers and solvents within (Angamma & Jayaram, 2016; Haider et al., 2015). A voltage rise past the critical point leads to beading of nanofibers due to the Taylor cone being too constricted while still trying to push through the same flow rate. Similarly, the flow rate has a critical point at which the polymer solution optimally forms nanofibers without deformation. Too high of a flow rate could create thicker nanofibers with higher porosity and ribbon-like morphology since the thicker diameters would require longer times to allow solvent evaporation and therefore have bigger pockets of solvent. Morphology can also be affected by the distance between the electrodes, also known as the needle to collector distance in this method of electrospinning, since these are generally what the electrodes are connected to. As distance between the collector and needle rises, the nanofibers have smaller diameters as well. On the other hand, too short of a distance does not allow proper nanofiber formation and raises diameter measurements (lowering Young's modulus measurements). The shortening of the gap allows less solvent to evaporate from the jet while the electric field application onto the nanofiber rises (since the electrodes are closer), leading to faster jets that could see minor diameter thinning. Therefore, a low enough voltage within the critical range helps create nanofibers optimally since it raises the

amount of time the jet is being suspended in the electric gradient but takes advantage of the stronger electric field to help thin out the nanofiber (Angamma & Jayaram, 2016; Haider et al., 2015).

Solution parameters could have just as much of an effect on final morphology of nanofibers. Ionic conductivity of the solution affects the jet diameter and could be optimized with salts or other polyelectrolytes due to there being more charge carrier concentration for the induced voltage to interact with (Miyamoto & Shibayama, 1973). Their presence also helps to shield the polymer chains from their own charge repulsion, compacting the nanofibers more uniformly (L. Li & Hsieh, 2005). The general relationship between conductivity and nanofiber diameter is that as conductivity of the solution rises, the diameter decreases. If the conductivity is too high though, the solution becomes more unstable and leads to higher bending instability and non-uniform nanofibers of varying diameters (Bhardwaj & Kundu, 2010; S. H. Tan et al., 2005). On top of reliance of conductivity on salts, variation of evaporating solvent in the solution could also affect the final morphology. More volatile solvents have higher evaporation rates, though quicker evaporation could mean that they leave the jet before too long into the jet elongation and create blockage on the needle tips from the dried solution (Haider et al., 2015). With low volatility (and therefore longer evaporation times), the nanofiber would not be dry enough by the time it reaches the collector and could lead to a mesh instead of individual fiber formation. Once a solvent is chosen, its effects on the viscosity or “gel-like nature” of the polymer solution must also be considered. If the viscosity is too low, the surface tension of the bead will have a harder time forming a proper jet and instead forms beads, or beaded jets. Higher viscosities give more uniform nanofibers with larger diameters but too high could clog the needle. Overall, every parameter is

interwoven and changing one affects many of the others. To study a certain complex, all aspects of the electrospinning apparatus should be considered for fabrication of uniform, tunable nanofibers.

2.1.2. Fabrication parameters for PAA:CS nanofibers. Our system of study included 0.1M FeCl₃ and 6M HCl solutions added to 0.568 grams 4.4% CS in 25% acetic acid and stirred for 30 minutes to get a homogeneous solution. After this, 1.43 grams of 35% PAA (Mw ~240,000, Sigma-Aldrich) were added to the above solution to make PAA:CS with mass ratio of 20:1. Different 0.1M FeCl₃ amounts were used to make Fe³⁺ metal ion concentrations 0.04%, 0.07%, 0.1%, 0.25%, 0.5%, 1% and 2% in solution by molar of the carboxylate group on PAA. To avoid gelation between Fe³⁺ and PAA, the pH was kept at 1 by addition of 6M HCl. Different amounts of deionized water kept the solution at total polymer concentration of 20%.

The above solution was loaded into a plastic syringe equipped with a 16 mm gauge needle made of stainless steel. The needle was connected to a high-voltage power supply, and solution was supplied continuously by a syringe pump. The electrospinning process was conducted in air at room temperature with voltages ranging between 10 and 12 kV. To obtain continuous and homogeneous nanofibers, voltages applied were adjusted during the process whenever necessary. The collector, a piece of aluminum foil, was placed 27 cm away from the tip of the needle (Malhotra et al., 2016). The as-spun nanofibers were dried at 40°C under vacuum and stored in a desiccator for later use.

2.1.3. Conductivity of pre-electrospun solutions. Ionic conductivity of the pre-electrospun nanofiber solutions is dependent of ions as the main charge carriers due to the nature of the polymers as polyelectrolyte materials as opposed to *electrical* conductivity which has electrons, ions, or a combination of both as charge carriers (Shetzline & Creager, 2014). Our system of study included 0.1M Samples of 6 grams of specific pre-electrospun polymer solution were placed in a 15mL EZ Flip™ conical centrifuge tube for conductivity studies. The measurements were obtained by a Thermo Scientific Orion 5 STAR A111 Benchtop Meter.

2.2. Scanning electron microscopy

SEM imaging utilizes an electron beam that interacts with the atoms of the sample and causes ejection of secondary electrons based off of topography and type of sample. The images seen are caused by detection of the secondary electrons in a rasterized pattern as the electron beam moves over the sample. A vacuum environment assures that the electron beam will only bounce off the sample and not air molecules in the sample chamber (Seiler, 1983). To satisfy the conductivity requirement of SEM, a conductive layer of metal (~10nm thickness) is applied over samples that are non-conductive or not conductive enough materials which could trap electrons and create bright spots in the image (Oatley, 1955).

Our study applied SEM (ZEISS ULTRA 55) for imaging on nanofibers electrospun on glass slides and coated in a thin layer of Au/Pb (Emitech k550). Working distance was between 6-10 mm and required 5 kV for imaging. Fiber diameter was measured through the scale bar on the images.

2.3. Infrared Spectroscopy

To better understand the results of nanofiber characteristics at different concentrations of metal ions, deeper study into structural morphology was done. Initial application of Fourier Transform Infrared (FTIR) spectroscopy was used to give a ‘fingerprint’ of pre-electrospun nanofiber solutions, with later application of atomic force microscopy infrared studies for more detailed understanding of the structural makeup of individual nanofibers.

2.3.1. Fourier Transform Infrared Spectroscopy. FTIR is the study of molecular bond vibrational frequencies through the application of infrared radiation and the resulting analysis of absorptions by the molecules. The structure and vibrational frequencies of the bonds and/or functional groups create a unique ‘fingerprint’ characteristic of that type of molecule (Coates, 2006). Functional groups, type of bonds (including twisting, stretching, etc.), and effect of nearby molecules all influence the final spectrum of the sample and allow for close study of changes in a system.

The infrared spectra of the PAA:CS nanofiber pre-electrospinning solutions were obtained using a Perkin Elmer Spectrum 100 series FT-IR spectrometer in the range of 600 to 4000 cm^{-1} with a resolution of 4 cm^{-1} and scan number of 4 to simulate the fibers. Nanofibers were too small for detection of signal and therefore vacuum-dried membranes of sample solution were used. None of the components were lost during the electrospinning process (simulated using vacuum drying on the solution).

2.3.2. Atomic Force Microscopy-Infrared Spectroscopy. NanoIR takes advantage of combining atomic force microscopy (AFM) that is capable of providing nanoscale resolution of physical properties with IR spectroscopy, which can elucidate chemical fingerprints of materials.

Initially discussed in 2000 by Hammiche et al. (Hammiche et al., 1999) and Anderson (Anderson, 2000), the rudimentary design consisted in mounting an AFM into the FTIR chamber. Upon illuminating the sample with IR light, vibrational modes in the material are excited by absorbing photons with energy required for the transitions. The energy absorbed upon excitation, is later released to the material in the form of heat. Such heat in the lattice leads to thermal expansion, which can then be detected with the AFM. Since the AFM cantilever is in direct contact with the sample, thermal expansion applies brief force (upward) to the cantilever tip. Due to the light pulse (similar to an impulse), this takes the form of ringing (large oscillations) at the cantilever's resonant frequencies. The cantilever motion is monitored using the readout laser being reflected off of the back of the cantilever and onto a photodiode detector. Once the IR light is off, the sample dissipates all the heat, and returns back to initial conditions (Anderson, 2000; Dazzi et al., 2012). Thus, the thermal expansion of the sample can be controlled by changing the pulse width or repetition rate of the excitation light (**Figure 5**). NanoIR imaging for this work was conducted with the cantilever in contact with the sample surface. The IR laser pulse was set to match the contact resonance of the cantilever. Two additional functions were considered for the data presented here: fixing the laser wavelength to a specific wavelength (remnant of FTIR peaks of interest) to generate a chemical map or by fixing the cantilevers position and sweeping the wavelength (1530 cm^{-1} to 1810 cm^{-1}) to obtain a localized IR spectrum.

For our study, sample preparation was modified to be considered optimal for nanoIR measurements. The fibers were deposited onto silicon wafers, selected due to absence of bands within the range of 1530 cm^{-1} to 1810 cm^{-1} . Wafers were cleaned in absolute ethanol by sonication bath for 2 h then rinsed by ddH₂O. In order to provide sufficient background for accurate IR

spectra, a half of each substrate was covered with aluminum foil during deposition to maintain a clean area for reference. Localized IR measurements were performed on a nanoIR2 platform (Anasys Instrument). The cantilevers selected for imaging were silicon n-type probes coated with gold on both sides. The associated contact resonance of the cantilevers used was 11-19 kHz with a force constant of 0.1-0.6 N/m. Imaging was collected at a constant scan rate of 1.0 Hz and at 500 by 500 pixels. For each sample multiple AFM images of the fibers was collected, as well as several IR spectra at various locations of the fibers fixed at 1710 cm^{-1} wavenumber, specific to PAA nanofibers. In cases where aggregates were observed, spectra on the fiber areas with and without aggregates were obtained to compare the composition.

2.4. Nanofiber bending mechanics analysis

While confocal microscopy allowed for the initial imaging of the PAA:CS nanofibers at different concentrations of ferric metal ions, further application of mechanical analysis was required. The idea of the nanofiber as a rod therefore, allowed use of the bending beam theory for calculation of mechanical characteristics.

2.4.1 Confocal microscopy imaging and persistence length analysis. Electrospun nanofibers were collected on microscope coverslips and visualized with an Olympus BX51M confocal dark field microscope equipped with a digital camera (Progres Gryphax model from Jenoptik) with a 20x objective. Filters were used to enhance nanofiber images on the microscope, including exposure filters for nanofiber brightness through lower gain filtration, color control, and high contrast. Low saturation and gamma values with high sharpness and noise reduction further allowed for clearer nanofiber distinction. Dark field microscope images were further processed for enhanced contrast and skeletonized using *ImageJ* software (NIH). *Persistence* software (Graham

et al., 2014) and *OriginPro 8* software were used to analyze the average length (L_{avg}) and bending persistence length (L_p) of PAA nanofibers (N=630-2200).

Nanofiber bending persistence length (L_p) was determined from the two-dimensional average angular correlation ($\langle C_s \rangle$) of the polymer tangent angles (θ) along the nanofiber segment length (s) as shown in Equation (1) for each chosen nanofiber before calculation of an overall average calculation of segment length (L_{avg}) and bending persistence length (L_p) (Graham et al., 2014).

$$\langle C(s) \rangle = \langle \cos[\theta(s) - \theta(0)] \rangle = e^{-s/2L_p} \quad (1)$$

The relationship of Equation (1) makes it so that if a nanofiber has higher stiffness, the angular correlation between the two endpoints of the contour length rises (**Figure 6**). This is due to thermal fluctuation not bending the filament as much and the fiber going a longer distance before the bending affects apply.

2.4.2 Beam theory for nanofiber bending mechanics and Young's modulus estimation.

Bending beam theory allows for the study of flexural rigidity and correlation with Young's modulus in a cross-section analysis of a beam bent by a controlled force. As the nanofiber bends, curvature in the rod is created. The application of force to the nanofiber is reflected in the bending moment (M) created by the curvature in the bend ($1/R$), with (R) representing radius of the curve of the nanofiber in Equation (2).

$$M = \frac{EI}{R} \quad (2)$$

Flexural rigidity takes into account Young's modulus (E) and second moment of inertia (I) of the nanofiber due to influence from the nanofiber's isotropic and homogenous nature and could be represented as flexural rigidity value (κ) in Equation (3) (Howard, 2001).

$$\kappa = EI \quad (3)$$

The theory depends on the assumption that the force is applied perpendicular to the beam. As the controlled force pushes on the nanofiber, the surface in contact with the applied force *contracts*, while the opposing face of the beam *extends*. At the center of the beam the forces of contraction and extension cancel out due to the force being perpendicular to the midpoint between both reactionary forces, creating a neutral plane within the bending nanofiber (**Figure 7**) (Kelly, 2013). It should be noted that such moment of inertia is based solely on geometry and therefore will only consider the influence of the Young's modulus and overall cross-sectional shape. A nanofiber can be assumed as a cylindrical rod, therefore the second moment of inertia is calculated from Equation (4), where (r) is the radius of a circular cross-section.

$$I = \frac{\pi r^4}{4} \quad (4)$$

Furthermore, establishing this relationship can be extended to take into account of the bending stiffness connection to Young's modulus through the flexural rigidity (κ) in the study of persistence length of the nanofibers in Equation (5), whereby the bending stiffness is represented by L_p and thermal energy ($k_B T$).

$$E = \frac{\kappa}{I} = \frac{L_p k_B T}{I} \quad (5)$$

Moment of inertia (I) of PAA nanofibers was calculated based on radius measurement from SEM images assuming a rod-like figure (**Figure 8A, B**) (McCullough et al., 2008; Nakielski et al., 2015; Ott et al., 1993). Scale of measurement was provided on the images. *ImageJ* software helped get diameter measurements by hand which were then converted from the pixel units to nanometers.

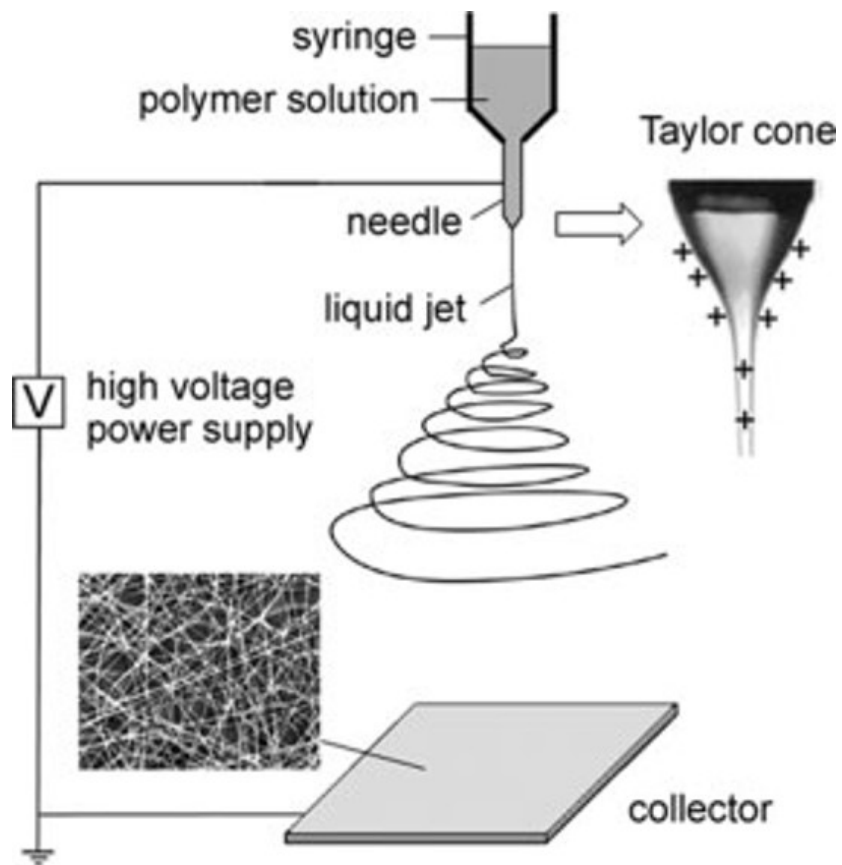


Figure 4. Electrospinning instrumentation setup. Polymer solutions are affected by the application of voltage and other controllable parameters. Image reference from: (D. Li & Xia, 2004).

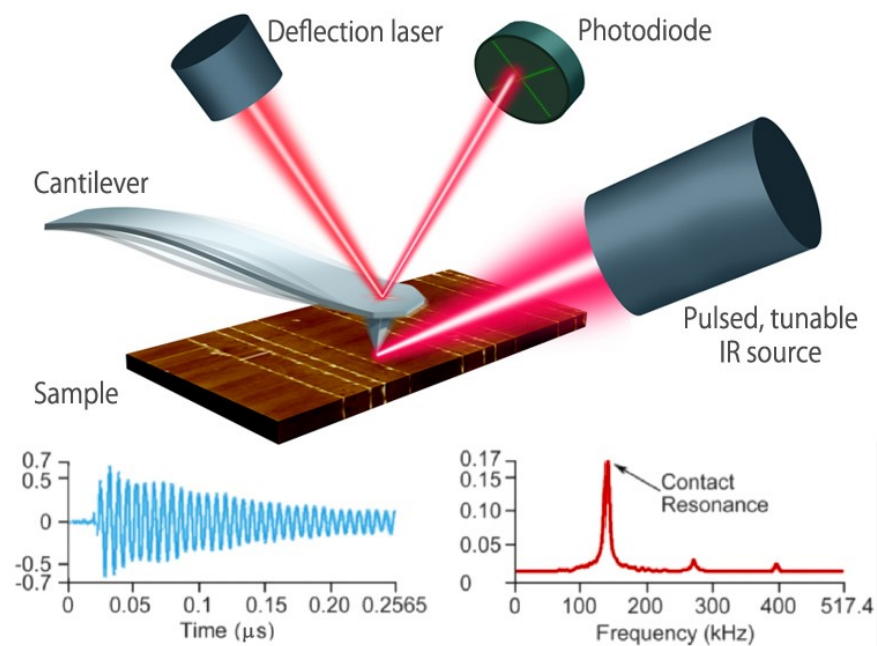


Figure 5. NanoIR setup schematic. AFM cantilever tip is in contact with sample which is placed on a silicon substrate. As the IR laser source excites the fibers, the cantilever captures the photothermal expansion of the material. Each pulse of IR light leads to cantilever ringing (blue curve). This is being detected using a read-out laser being bounced off of the back of the cantilever and onto a detector. The ringing is Fourier transformed to obtain the frequency spectrum (red). The amplitude of the contact resonance peak is recorded to obtain the NanoIR spectra or images. Image reference from: (Dazzi et al., 2012).

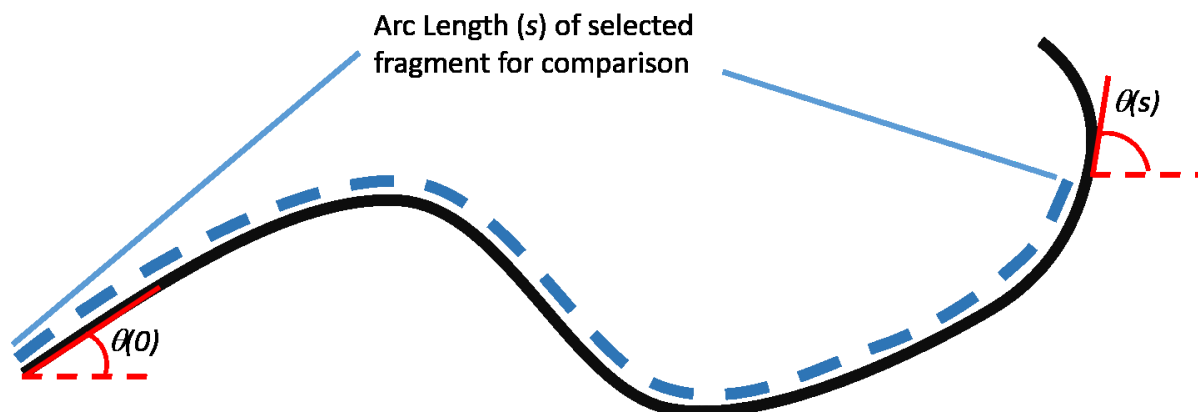


Figure 6. Measurement of bending stiffness in nanofibers relies on correlation analysis between chosen endpoints. *Persistence* software takes measurements at multiple points along the length of the nanofiber to build L_p analysis, which can then be applied in *OriginPro* calculations of angular correlation.

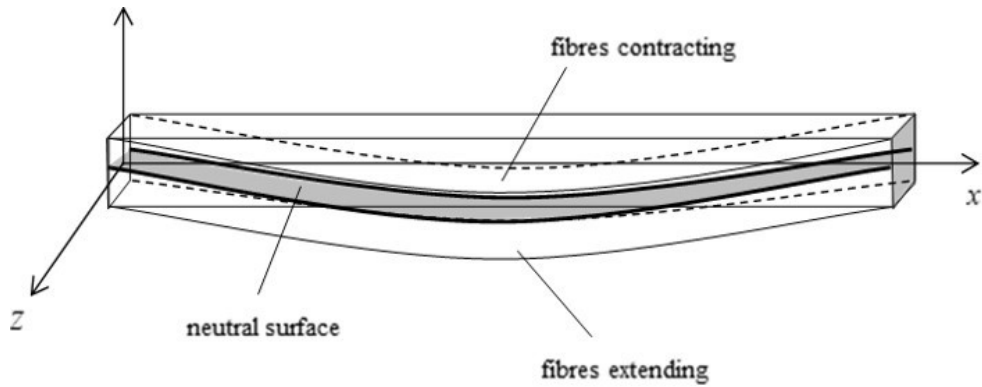


Figure 7. Bending beam theory application for nanofiber Young's modulus measurement. As a fiber bends, one side has applied force and contracts to create a shorter edge, while the corresponding opposite side undergoes an extension. The neutral surface is assumed parallel to the applied force and has no contractile or extension forces affecting it since they cancel out in that plane. Image reference from: (Kelly, 2013)

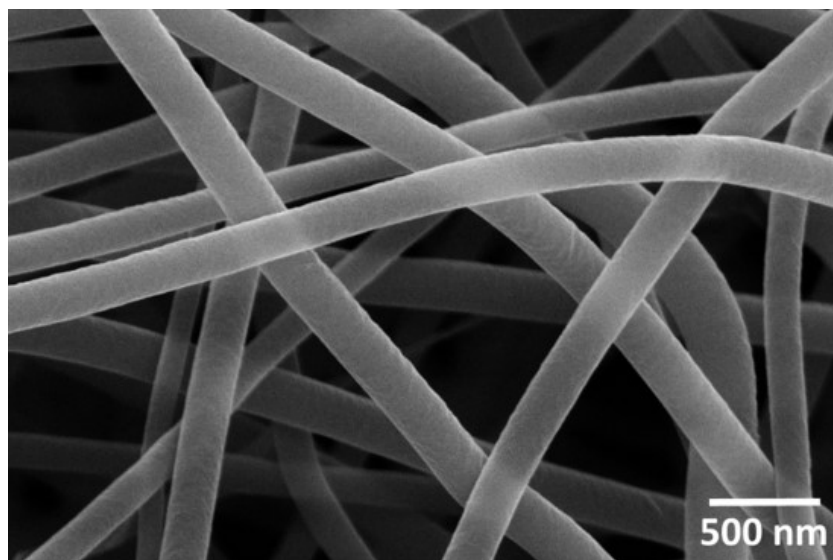


Figure 8. Representative images of PAA:CS nanofiber SEM. Measurement of diameter was used in calculations of individual nanofiber second moment of inertia, which could then be used to estimate Young's modulus measurements.

CHAPTER THREE: RESULTS

3.1. Ferric ions modulate the mechanical properties and average length of polyacrylic acid nanofibers.

Imaging of PAA:CS nanofibers revealed initial indication of changes induced by the addition of ferric metal ions to the complex (**Figure 9**). Application of the images to analysis via *Persistence* and *OriginPro* software helped determine that ferric metal ions did have a pattern of effect on PAA:CS nanofibers. The bending persistence length (L_p) estimation was based off of Equation (1) considering two-dimensional nanofiber segment length in relation to angular correlations (Graham et al., 2014; McCullough et al., 2008), which have successfully captured semi-flexible biopolymer mechanics (**Figure 10**).

Ferric ions affected the bending stiffness and average lengths of PAA:CS nanofibers through electrostatic interactions (**Figure 11**). Controlled variations of ferric metal ion concentrations led to qualitative effect on the flexibility of nanofibers in a non-linear pattern (N=630-2200) (**Figure 12A**). The control samples had an average bending stiffness starting out at 66.59 μm . Comparison with 0.04% ferric concentration samples of PAA:CS nanofibers (81.30 μm) showed that the bending stiffness of fibers without metal ions had markedly higher flexibility (correlated with lower bending stiffness values). At 0.07% ferric concentration, the stiffness of the nanofibers dropped by about 17% to 67.42 μm in comparison with 0.04% ferric samples. Further addition of ferric metal ions (0.10% concentration) to the PAA:CS complex prior to electrospinning dramatically raised the average bending stiffness of nanofibers to 121.96 μm , the *highest* bending stiffness achieved from all the attempted concentration variations of ferric metal ions. Raising the concentration of metal ions further to 0.25% ferric yielded the *lowest* average L_p of our samples at

62.29 μm , and therefore fabrication of the most flexible of all nanofibers. Continuing to 0.50% ferric metal ion concentration of PAA:CS nanofibers brought the bending stiffness back up to 86.65 μm , slightly higher than the nanofiber measurement obtained at 0.04% concentration. Further addition of ferric metal ions did not affect the bending stiffness as much as previous lower variations. With ferric metal ions at 1.00%, the average bending stiffness only lowered to 82.33 μm . Finally, at 2.00%, the effect of metal ions reached 78.92 μm , showing that at the three highest concentrations the flexibility of the nanofibers only minorly changed. Bending stiffness range of measurements was widest for 0.10% ferric samples as revealed in box plot graphing, spanning from about 75 μm to 230 μm while none of the other data plots broke past a bending stiffness higher than about 135 μm (**Figure 12B**).

Length changes brought on by ferric metal ions also showed a non-linear pattern of effect (**Figure 13A**). PAA:CS nanofibers rose in average length from 95.7 μm (0% Fe^{3+}) to 52.9 μm (0.04% Fe^{3+}). Though the change between the control and initial concentration was a loss of length of about 55%, the following concentrations did not show as marked a change. Raising the concentration further to 0.07% lowered the average PAA:CS fiber lengths to 46.56 μm , and further addition of ferric (0.10%) only shortened the nanofibers to an average length of about 44.07 μm . This is one of the shortest average lengths accomplished out of all concentrations. Further study of the range of measurements via box plot application revealed that nanofiber length measurements varied mostly at a concentration of 0.25% (**Figure 13B**), where a lengthening of the nanofibers to 77.51 μm occurred, the longest average attained in our studies with addition of metal ions. Continuing to 0.50% concentration, the nanofibers did get shorter, though the change was not as drastic (65.68 μm). The final two concentrations showed a further shortening, the length

measurements came out very similar. The 1.00% samples had an average length of 37.91 μm , while 2.00% showed a slightly longer length of 38.31 μm .

3.2. Chitosan helps ferric ions modulate the mechanical properties of PAA nanofibers.

To identify the roles of chitosan in PAA nanofiber mechanics, we imaged PAA nanofibers in the presence or absence of chitosan and measured nanofibers' lengths and bending persistence lengths through the same methods as those from the previous section at varying ferric metal ion concentrations.

Overall, nanofibers with chitosan showed less change in length and ranged from half to three times shorter than their non-CS PAA counterparts (**Figure 14A**). At a concentration of 0.04% Fe^{3+} , chitosan nanofibers showed a length of 52.94 μm compared to PAA without CS (at 0.04% Fe^{3+}) average length of 156.65 μm . At the slightly higher 0.07% ferric concentration, CS-containing nanofibers had an average length of 46.58 μm , being nearly half of the length of nanofibers without CS (100.47 μm). This pattern was also repeated with the higher concentration of ferric (0.10%), with PAA:CS lengths averaging at 44.07 μm as compared with PAA nanofibers with lengths of 88.55 μm . Control samples of nanofiber length with PAA:CS had average length of about 95.74 μm but could not be directly compared to their non-CS counterparts due to the nanofibers spanning much longer lengths than the imaging parameters allowed for measurement. The box plot analysis of the nanofibers revealed that the most varied range of lengths occurred at a concentration of 0.04% ferric metal ions without chitosan, spanning from under 25 μm to slightly under 350 μm (**Figure 14B**).

Bending stiffness effects of CS on PAA nanofibers with Fe^{3+} were not as easy to discern as the length patterns (**Figure 15A**). PAA:CS had a higher bending stiffness of 81.30 μm compared to

non-CS nanofibers at average bending stiffnesses of 66.94 μm , indicating more flexibility without CS. At 0.07% ferric metal ions, the CS nanofibers become more flexible with a bending stiffness of 67.42 μm compared to the higher one of non-CS at 78.03 μm . Interestingly, the 0.10% samples (no CS) affected the persistence length about the same as those with the same concentration of ferric and chitosan included with bending stiffness measurements of 125.95 μm and 121.96 μm respectively. In box plot analysis of the measurements, chitosan nanofibers showed a wider range (about 76-220 μm) than non-CS samples (80-200 μm) (**Figure 15B**). Control nanofiber measurements were also attempted, though the measurements of those without CS could only be done on segments as opposed to end-to-end measurement due to imaging constrictions (as stated in previous paragraph). As such, bending stiffness of nanofibers without CS (47.66 μm) was most likely lower. PAA:CS nanofiber bending stiffness recall, was at 66.59 μm and therefore showed CS making the complex stiffer than the non-CS nanofibers.

3.3. Electrospun PAA:CS nanofiber Young's modulus is affected by ferric metal ion.

We estimated the Young's modulus (see Methods for details) of PAA:CS:Fe³⁺ nanofibers based on average persistence length analysis and diameter measured from SEM images. Young's modulus in our study ranged from 0.27 kPa to 16.51 kPa (**Table 1**). The nanofibers with highest calculated strength were at a ferric concentration of 0.10% with chitosan.

Nanofibers with CS tended to range from below 1 kPa to about 4 kPa of average Young's modulus, with exception of 0.10% ferric concentrated samples which had the lowest diameter and therefore the highest calculated range limit of Young's modulus at 16.51 kPa. Control samples with chitosan had a Young's modulus of 3.25 kPa at an average diameter of 202 nm, while PAA-only nanofibers showed a much lower average strength at 1.10 kPa in correlation with their higher

average diameter of 235 nm. The lowest values of strength of the measured concentrations were from 1.00% ferric metal ion concentrations ranging from their lowest average at 0.27 kPa, to a much higher 3.36 kPa.

3.4. Characterization sheds light on how ferric metal ions affect individual PAA:CS nanofiber structure.

Metal ion interaction at varying concentrations influences bonds of polyacrylic acid in individual nanofibers. According to FTIR spectra, free carboxyl groups of PAA have a sharp band at 1702 cm^{-1} , indicating a strong C=O stretching vibration and the low concentration of Fe^{3+} that attached to these groups (**Figure 16A**). For comparison, strong C=O stretching vibration for monomer carboxylic acid is at $1770\sim 1750\text{ cm}^{-1}$ while for PAA this peak is displaced to a lower wave number because of hydrogen bonding among the carbonyl groups of the polymer (Hoerter et al., 2008; Kim et al., 2007; Todica et al., 2015). This peak was further shifted due to reconfiguration of polymer chains post- Fe^{3+} addition (Hoerter et al., 2008; Kim et al., 2007).

Interestingly, in FTIR a peak at 1591 cm^{-1} only appeared for samples with a ferric concentration at 1% showing carboxyl C=O asymmetric stretching. Since symmetric stretching of the carboxyl groups on PAA are at 1412 cm^{-1} , the difference between this peak and the asymmetric one in 1% ferric metal ion samples is 179 cm^{-1} . According to Kirwan et al., comparison of the distance between symmetric and asymmetric stretching ($\Delta\nu$) compared to salt ($\Delta\nu_{\text{salt}}$) helps determine the type of bond between the carboxylate groups and metal ions (Kirwan et al., 2003). This value is larger than the $\Delta\nu$ for PAA:CS nanofibers indicated by Malhotra et. al's values, therefore showing that the type of bonds between PAA and Fe^{3+} are due to bidentate bridging in that concentration of ferric (Baigorri et al., 2007; Malhotra et al., 2016). The 1% concentration

also displayed a sharper, slightly larger peak of 1412 cm^{-1} owing to more symmetric carboxyl group vibrations than in the other samples. And though the peak at 1169 cm^{-1} is present across all samples, it is higher at 1% ferric metal ion concentration and is due to the stretching of neighboring carboxyl groups (Baigorri et al., 2007). These peaks are further sharpened as the concentration rises to 1.5% and 2%, though the highest peaks are displayed at 1.5% of ferric concentration, followed by 2%. Raising the concentration of metal ions to 5% leads to a significant change, raising the transmittance across all peaks.

The rise of a peak at 1452 cm^{-1} represents C-H deformation with increasing Fe^{3+} concentrations and therefore rearrangement of the system. Further C=O stretching coupled with O-H in-plane bending is reflected in the peak at 1233 cm^{-1} but does not see major change across concentrations. Nonetheless, this peak does suggest that PAA is a polymer with syndiotactic configuration in which repeating units alternate stereochemical configuration in a regulated manner. Had it been atactic (lacking regular stereochemical configurations), there would have been a peak at 1250 cm^{-1} , as well as a shoulder at 1300 cm^{-1} (Dong et al., 1997). The peak at 1169 cm^{-1} , according to Baigorri et al. indicates C=O stretching of neighboring carboxyl groups (Baigorri et al., 2007). It remains clearly defined across all samples, though it does weaken slightly with the rising concentration of ferric.

Previous work states that the chitosan interaction with the ferric metal ions and PAA is minimal due to the pH of the solution being low, leading to protonation of CS chains and not allowing for further interaction with the system (Guibal et al., 2014). Protonation effect was somewhat verified by the PAA-CS- Fe^{3+} FTIR data, which is similar to past characterization of PAA- Fe^{3+} systems with no chitosan characteristic peaks at 1154 cm^{-1} or 893 cm^{-1} present (Su et al., 2011). Further

literature search did indicate peaks at 1601 cm^{-1} and 1650 cm^{-1} for the depicting of N-H bending in primary amino groups as well as carbonyl stretch of amide bonding (Su et al., 2011) which were not initially noted as an issue in FTIR until peak deconvolution studies revealed new peaks (see below). Direct verification of Fe-O interaction bands would have to be on FTIR with lower range, seeing as they appear below 500 cm^{-1} and therefore outside the scope of our instrument (Baigorri et al., 2007).

Further study into concentrations of PAA-only, 0.04%, 0.10%, and 1.00% of ferric metal ion peak deconvolutions within the wavenumber range of $1530\text{-}1810\text{ cm}^{-1}$ (**Figure 16B-E**) indicate the splitting of the peak at 1702 cm^{-1} into a peak at 1668 cm^{-1} and 1710 cm^{-1} . FTIR deconvolution of PAA-only samples (**Figure 16B**) reveal only the two peaks mentioned above. According to Zheng et. al, the 1668 cm^{-1} peak is indicative of asymmetric stretching of the carboxyl groups of PAA (Zheng et al., 2016), though to our knowledge further comparisons could not be justified with literature due to no mention of such a peak. The remaining 1710 cm^{-1} peak reveals further C=O stretching of the carbonyl (Anjum et al., 2017) as well as intermolecular hydrogen bonding of the carbonyl groups . These two peaks remain present through the other samples but shift in size. In the 0.04% sample the 1668 cm^{-1} peak has less height, but the 1710 cm^{-1} peak is larger (in comparison to both the PAA-only 1710 cm^{-1} peak as well as the 1668 cm^{-1} in the same concentration), showing more stretching of C=O carbonyl bonds and hydrogen bonding (**Figure 16C**). Further addition of ferric metal ions to create the 0.10% FTIR spectra for deconvolutions reveal a shift once again in size, though there was no change in the type of peaks (**Figure 16D**). The peak at 1668 cm^{-1} had a higher value than any of the previous concentrations, while 1710 cm^{-1} became smaller. Peaks at the 1.00% (**Figure 16E**) had more shifting still and revealed several

more peaks not seen in the lower concentrations, including 1591 cm^{-1} , 1637 cm^{-1} , 1727 cm^{-1} , and 1753 cm^{-1} . The type of bridging seen for ferric metal ions was studied using the 1591 cm^{-1} peak initially, though further deconvolution with AFM-IR application have revealed more detail into the bridging studies done through FTIR peaks (see below). Polyacrylic acid peaks at 1637 cm^{-1} verify asymmetric vibrations of PAA (Zhong et al., 2015b), while 1727 cm^{-1} shows C=O stretching of the carboxyl groups (Singh & Singhal, 2012). Though there is a lack of more indicative peaks at lower concentrations, it could be due to the small amount of metal ions in solution and therefore less interactions. The further study of these concentrations with AFM-IR is therefore meant to offer better insight into the bond vibrational changes occurring.

Application of AFM-IR at the same concentrations (PAA-only, 0.04%, 0.10%, and 1.00% Fe^{3+}) as FTIR peak deconvolutions takes advantage of higher spatial resolution to allow better study of the morphological changes, including imaging of topography and clustering (**Figure 18A**, **18B**). PAA-only nanofibers are used as control samples to show clustering of ions was only occurring in the nanofibers with metal addition, as well as including further reference peaks (**Figure 18C**). However, comparison with nanoIR peaks shows further deconvolution with an extra peak at 1727 cm^{-1} (**Figure 18G**), seen in the FTIR results only in the 1.00% concentration. The samples with metal ion concentrations were more thoroughly studied via their breakdown into the nanofiber as well as cluster deconvoluted spectra. At a concentration of 0.04% metal ions (**Figure 18D**), the same peaks seen in PAA nanofibers were present, though there was a shift in height for the 1668 cm^{-1} and 1727 cm^{-1} peaks showing the influence of the metal ions even at small concentrations. Cluster studies for the 0.04% concentration (**Figure 18H**) show further peaks at 1620 cm^{-1} and 1691 cm^{-1} but did not contain the peak at 1727 cm^{-1} , which means there is less C=O

stretching of the carboxyl groups. The peak at 1620 cm^{-1} is due to asymmetric stretching of PAA (Anjum et al., 2017), revealing the interaction with the ferric metal ions. At 1691 cm^{-1} , it appears that the PAA carbonyl groups of monomers have conformational changes induced by the metal ions to the polymer chains (Dehghani et al., 2017). Comparison of the changes at 0.10% Fe^{3+} (**Figure 18E**) reveal a new peak at 1650 cm^{-1} , though it is not fully clear how much is influence from the chitosan (J. W. Lee et al., 1999; Smitha et al., 2004; Su et al., 2011) versus the C=O bonds of PAA (Baigorri et al., 2007). The peak at 1710 cm^{-1} becomes smaller while 1727 cm^{-1} peak rises, though it is the opposite in the cluster peaks (**Figure 18I**). Clusters at 0.10% ferric metal ions have two additional peaks at 1571 cm^{-1} and 1704 cm^{-1} . The conformational changes of the monomers of PAA at 1691 cm^{-1} are much more apparent in 0.10% in comparison to the clusters at 0.04% ferric concentration, showing higher strain as more bonds are being formed within the nanofiber structure. The final peak within the 0.10% cluster spectra at 1704 cm^{-1} could be due to intermolecular hydrogen bonding occurring amongst carbonyl groups of the PAA (Hoerter et al., 2008; Kim et al., 2007; Todica et al., 2015) which is more possible as the polymer chains are wrapped tighter around the ferric metal ions. At the final concentration studied ($1.00\% \text{Fe}^{3+}$), the widest variety of peaks is present. In the nanofiber (**Figure 18F**), the 1650 cm^{-1} peak is barely present in comparison to the 0.10% ferric nanofiber spectra. This could be due to further protonation of chitosan or less C=O bond vibrational changes. This is one of two peaks which is not present in the cluster of 1.00% nanofibers (**Figure 18J**), the other of which is the peak at 1668 cm^{-1} (indicating lowering of asymmetric stretching). Nonetheless, presence of peaks at 1571 cm^{-1} and 1620 cm^{-1} verify ferric interaction with PAA and bidentate bridging. The presence of the remaining peaks (1691 cm^{-1} , 1710 cm^{-1} , and 1727 cm^{-1}) show that the main interactions occur with

the polyacrylic acid, though further verification of lack of chitosan bond vibrations is required to confirm this.

Finally, there are peaks at about 800 cm^{-1} indicative of C-H twisting on PAA as well as C-COOH stretching (Dong et al., 1997). Though clear across all samples, the effect is strongest at 1.5% ferric concentration, further confirming the higher reconfiguration effect occurring within the system when compared with other concentrations.

Conductivity of the nanofiber system was also studied. PAA and CS individually show a very low level of conductivity (**Figure 19**). Addition of HCl raised the measurement to 83.2 mS/cm, but the value barely changed with addition of 0.04% ferric metal ions. Ferric at a concentration of 0.1M showed the highest conductivity by itself with values of the mixed nanofiber solutions never rising as high. When the same concentration of ferric was used without chitosan, the conductivity dropped slightly. The final concentration tested (1%) did not show significant change from the conductivity of 0.10% ferric metal ions. Overall no real conductivity differences could be used definitively to differentiate one concentration from another.

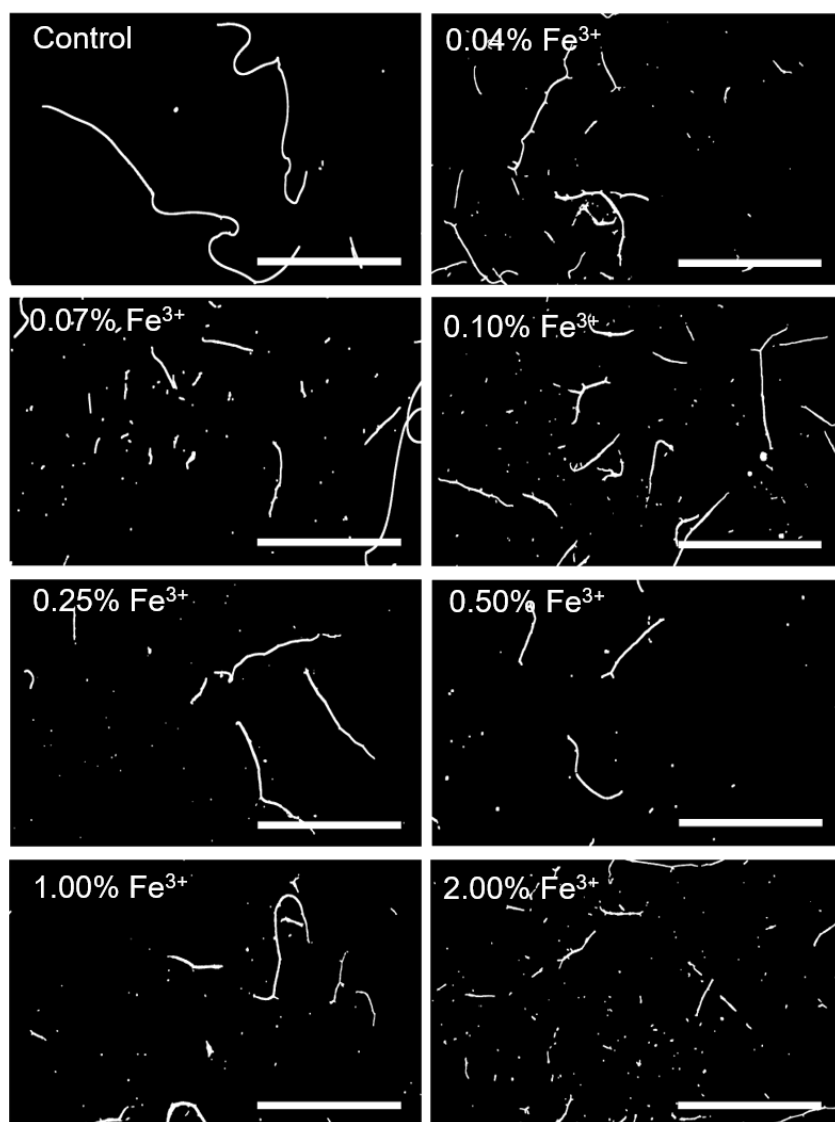


Figure 9. Representative dark field confocal microscopy images of electrospun PAA:CS nanofibers at varying ferric metal ion concentrations (0%, 0.04%, 0.07%, 0.10%, 0.25%, 0.50%, 1.00%, 2.00%). These reveal qualitative changes in length and stiffness of nanofibers at different ferric metal ion concentrations. *ImageJ* is used to create a skeletonized version of the nanofibers which is overlaid on filter-enhanced contrasted images in *Persistence*. Accurate end to end determination via *Persistence* selection is verified by user for final calculation of average length and bending persistence length of set. Scale bar represents 300 μm .

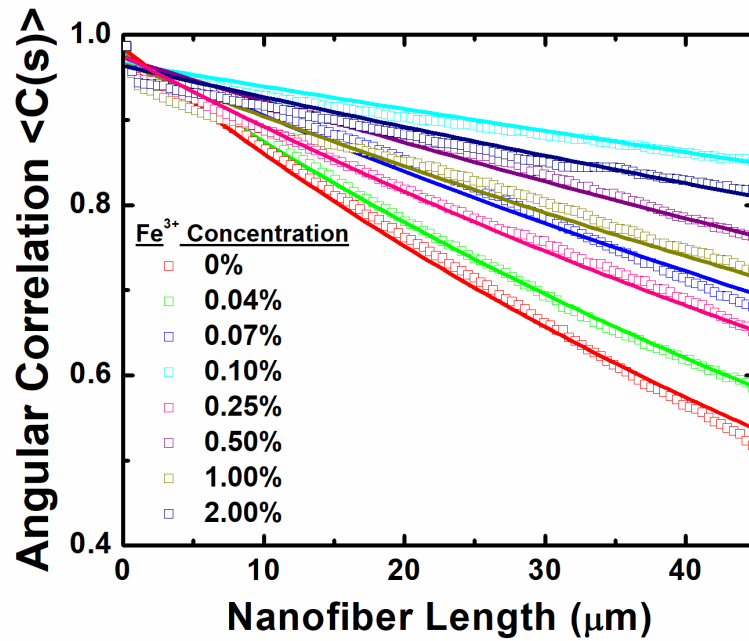


Figure 10. The cosine correlation functions are plotted against PAA:CS nanofiber segment length at varying ferric ion concentrations. Solid lines indicate best fits of the data in accordance to Equation (1), yielding the bending persistence lengths. Changes in ferric concentration affect bending stiffness of nanofibers.

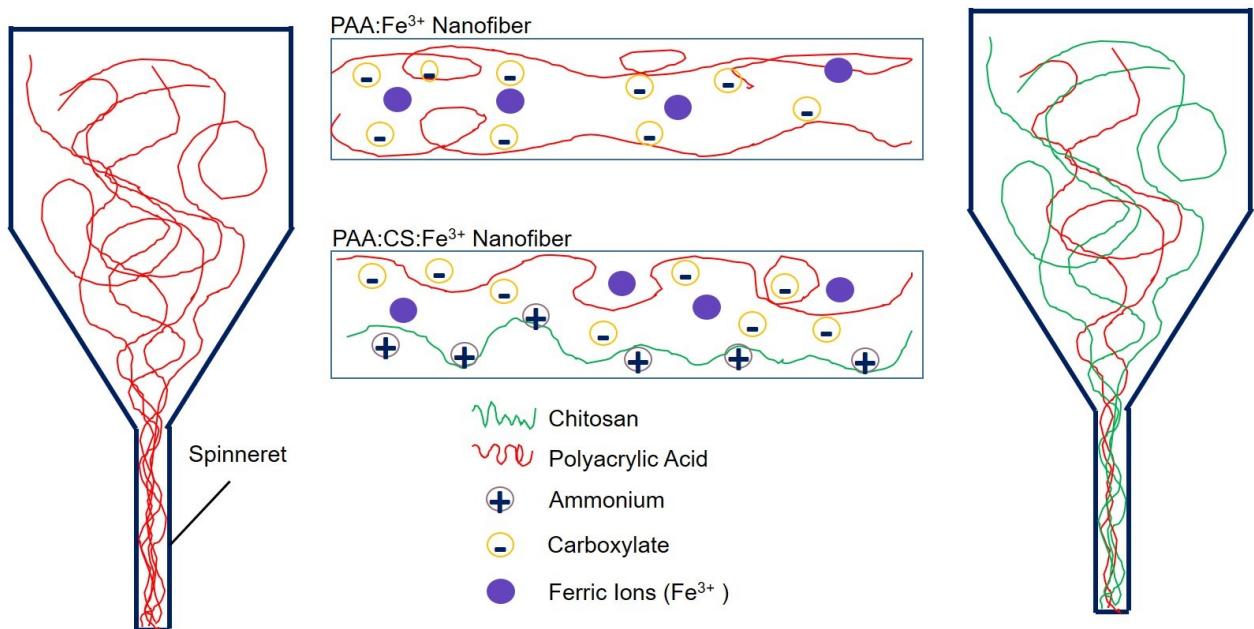


Figure 11. Electrostatic interaction schematic of PAA with CS and ferric metal ions. PAA anionic carboxylate groups form electrostatic crosslinks with CS cationic amine groups and metal ions for further nanofiber stability.

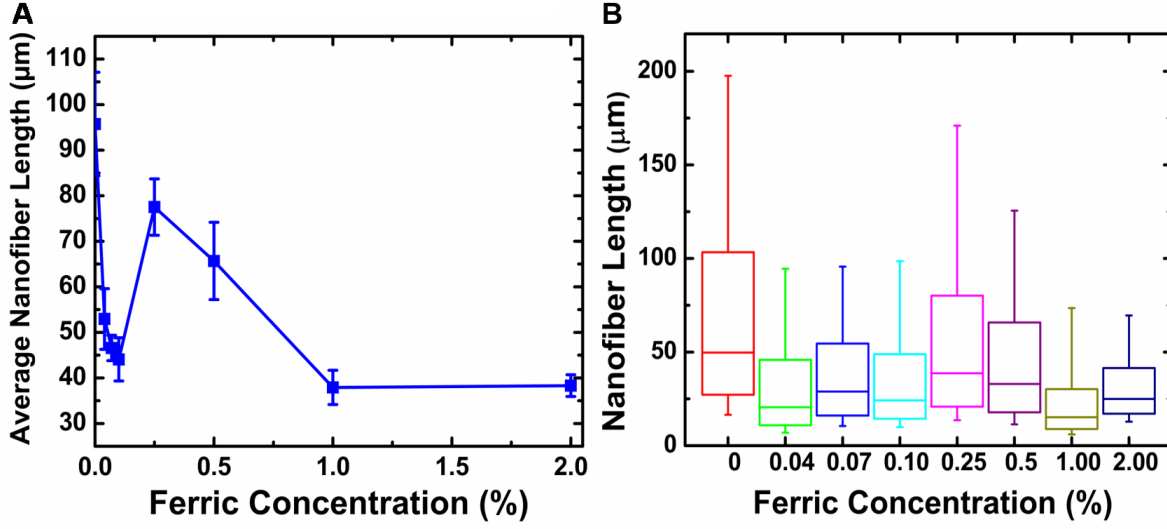


Figure 12. Ferric metal ions influence nanofiber length in a nonlinear manner. (A) Average nanofiber length depends on ferric ion concentration. The shortest nanofibers at the lowest possible concentration are created at 0.10% ferric metal ions, with ion effects also revealing a non-linear pattern of effect. (B) Box plot of nanofiber length distribution at varying ferric ion concentrations. Though 1.00% and 2.00% concentrations show some of the shortest nanofibers, this seems to be at the threshold of effect metal ions can induce. Range of lengths at lower concentrations do not show a large difference until the 0.25% concentration, suggesting a level of optimization before further shifting of ferric in the system. The box range represents quartiles of 10% and 90% and reveals the effect of ferric concentration strength on each set. (N=630-2200)

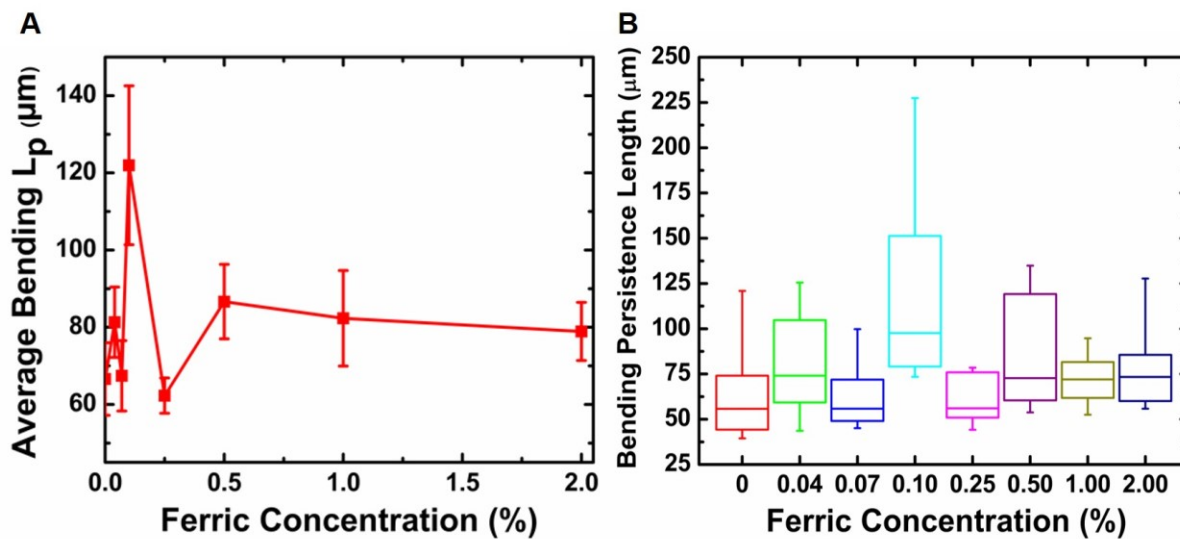


Figure 13. Ferric ion modulation of bending stiffness in PAA:CS nanofibers is determined by persistence length analysis. (A) Ferric ion-dependent bending persistence length of PAA:CS nanofibers. With addition of ferric, that interaction between metal ions and PAA:CS raises stiffness of the nanofibers in a non-linear manner. (B) The box range represents quartiles of 10% and 90% and reveals ferric modulation distribution. Metal ion concentration of 0.10% has the most effect on nanofiber stiffness and shows the widest range in distribution of effect. (N=630-2200)

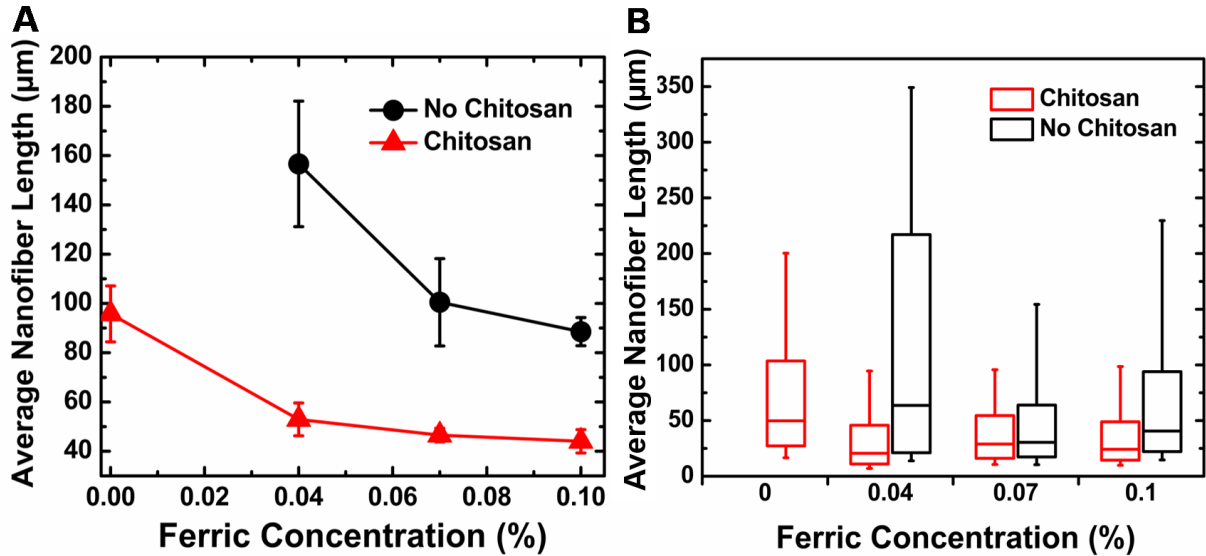


Figure 14. Comparison analysis of length of nanofibers electrospun with and without chitosan at initial concentrations 0%, 0.04%, 0.07%, and 0.10% of ferric metal ions. (A) Nanofibers with no chitosan (circles) show a higher average nanofiber length that falls dramatically as the concentration of ferric rises. Nanofibers with chitosan (triangles) did have measurable lengths that began well below estimations for PAA only nanofibers, and therefore showed more overall stability in length changes. (B) Length distribution comparison. The box range represents quartiles of 10% and 90% and reveals the effect of ferric metal ions and chitosan on each set. Nanofibers with no chitosan (black) show a wider variation of lengths than nanofibers with chitosan. A box was not created for nanofibers with no chitosan due to their lengths surpassing imaging limitations.

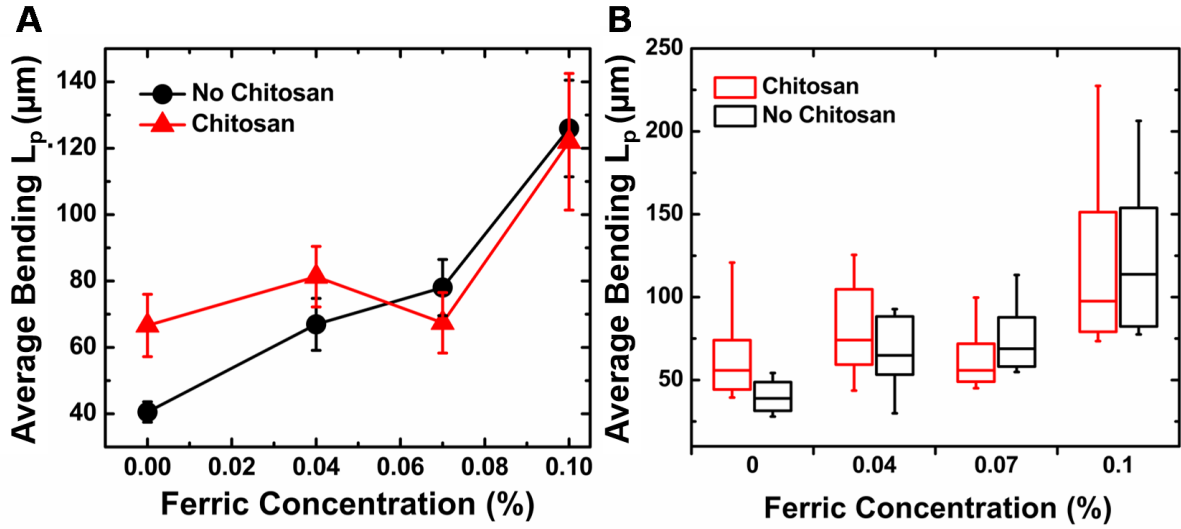


Figure 15. Comparison analysis of nanofiber bending stiffness of nanofibers electrospun with and without chitosan at concentrations 0%, 0.04%, 0.07%, and 0.10% of ferric metal ions in box plots. (A) Nanofibers with no chitosan (circles) at 0%, 0.04%, and 0.07% concentrations of ferric have lower persistence length and therefore bending stiffness than the average nanofiber with chitosan (triangles). At concentration 0.10% of ferric, both nanofibers with and without chitosan converge at similar persistence length averages, as well as highest impact concentration of ferric on overall stiffness of the nanofibers. Bending stiffness measurements on PAA-only nanofibers were acquired on fragments of nanofibers that could be captured in span of image. (B) Nanofibers with no chitosan (black) mostly have lower persistence length and therefore stiffness than the average nanofiber with chitosan (red). At concentration 0.10% of ferric, both nanofibers with and without chitosan converge at similar persistence length averages, as well as highest impact concentration of ferric on overall stiffness of the nanofibers. Bending stiffness of nanofibers without chitosan or ferric were obtained on filament fragments that fit within the imaging window.

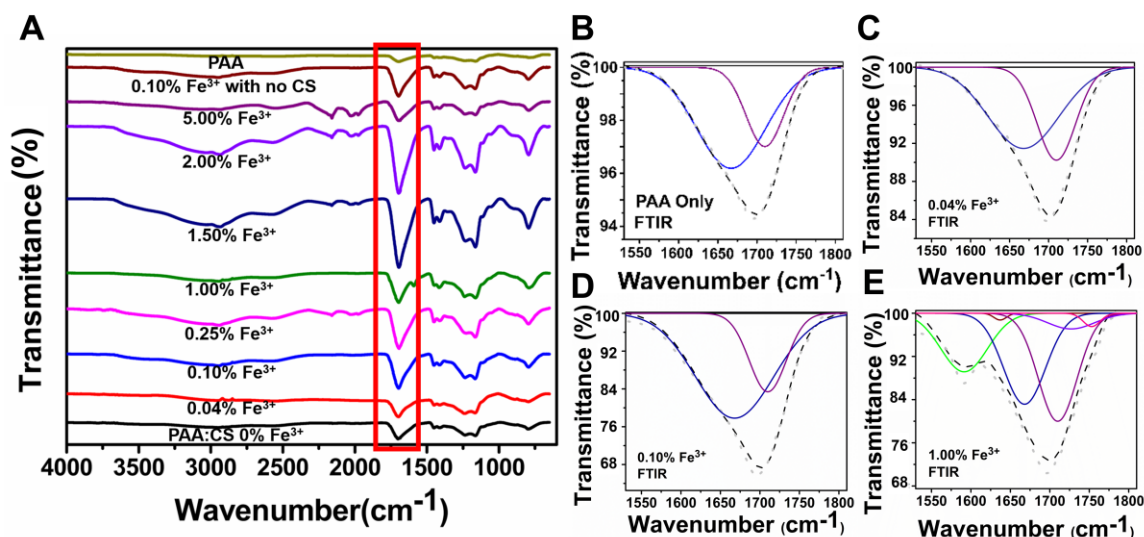


Figure 16. Nanofiber Fourier Transform Infrared (FTIR) spectra (A) at varying ferric concentrations and (B-E) peak deconvolutions at a range of 1530-1810 cm^{-1} . A) PAA bonds with Fe^{3+} are reflected in carboxyl group peak shifts. The peaks at 1702 cm^{-1} , 1452 cm^{-1} , 1412 cm^{-1} , 1233 cm^{-1} , 1169 cm^{-1} , and 800 cm^{-1} show the strongest interaction between the metal ions and PAA at 1.50% ferric concentration. However, only at samples with 1.00% ferric is a single peak indicating asymmetric stretching of carboxyl groups of PAA present. Further studies were done through peak deconvolution of the spectra within the range of 1530-1810 cm^{-1} . B) Peak deconvolution of PAA-only nanofibers revealed peaks at 1668 cm^{-1} (royal blue) and 1710 cm^{-1} (purple) within the 1702 cm^{-1} peak seen in FTIR. In both 0.04% (C) and 0.10% (D) concentrations of Fe^{3+} , no further peaks are found. E) At 1.00% Fe^{3+} , a peak is verified at 1591 cm^{-1} (green) indicating possible bidentate bridging, with further peaks at 1637 cm^{-1} (small dark red peak), 1727 cm^{-1} (light purple), and 1753 cm^{-1} (pink). The peak at 1637 cm^{-1} shows asymmetric stretching of carboxyl groups. 1727 cm^{-1} and 1753 cm^{-1} show strong C=O stretching of free carboxyl groups.

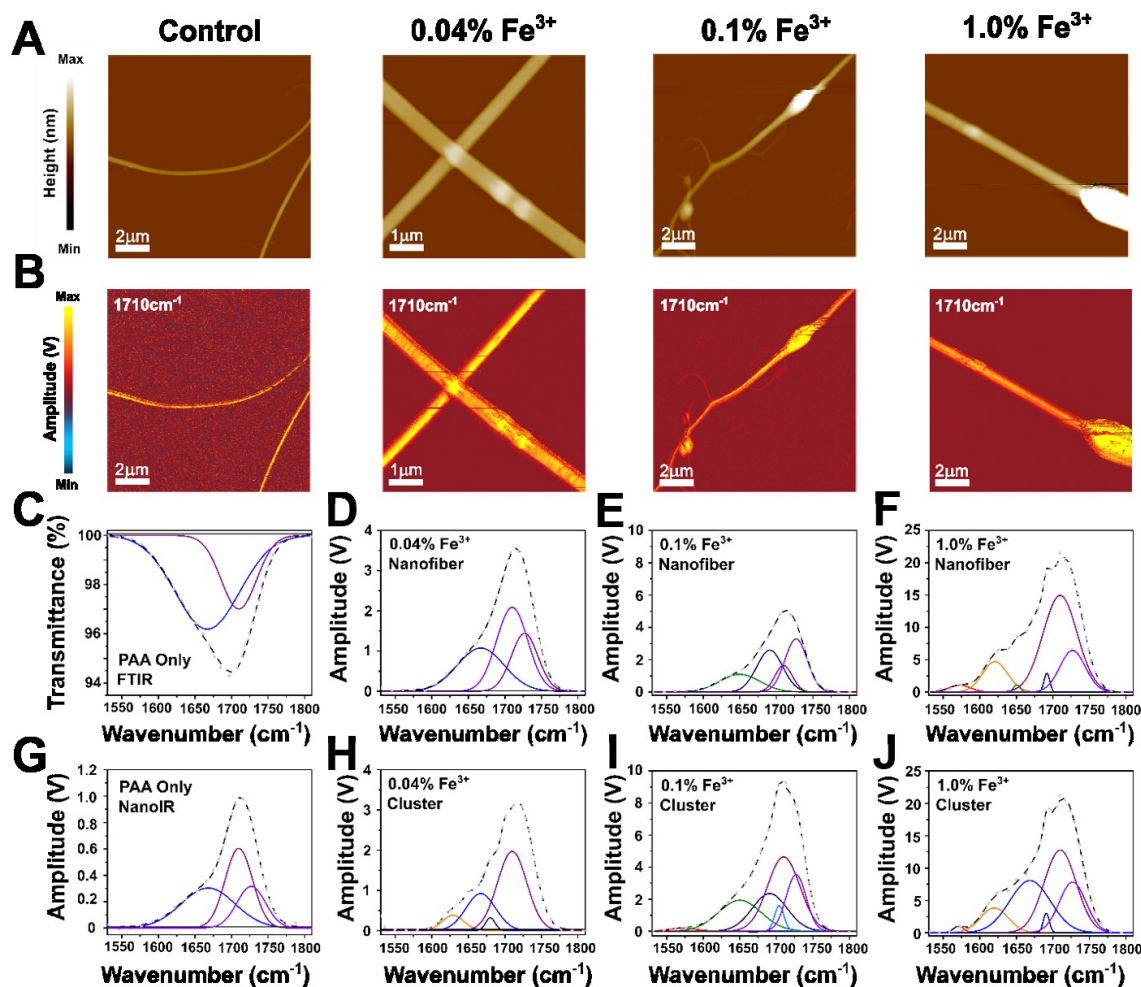


Figure 17. AFM-IR studies of nanofibers at 0.04%, 0.10%, 1.00%, as well as control nanofibers (PAA only). A) AFM height images of nanofibers at varying concentrations on silicon substrates. B) Images of nanofiber topography across the different concentrations reveal clustering of metal ions. C) Peak deconvolution on PAA-only nanofibers in FTIR indicating the main reference peaks used for further peak deconvolution in nanoIR spectra. D-J) Deconvolution of the peaks across the wavenumber range of 1530-1810 cm^{-1} reveals the molecule vibrations at both the nanofiber and clusters formed by the ferric metal ions. Peaks at 1571 cm^{-1} (red), 1620 cm^{-1} (orange), 1668 cm^{-1} (cobalt blue), 1691 cm^{-1} (navy blue), 1704 cm^{-1} (denim blue), 1710 cm^{-1} (purple), and 1727 cm^{-1} (violet) are not all present across both nanofibers and clusters. Indication of ferric metal ions forming bidentate bridging is verified via the formation of the peaks at 1571 cm^{-1} and 1620 cm^{-1} . The presence of chitosan cannot completely be verified but could be indicated by the 1650 cm^{-1} peak (green), though only in the 0.10% nanofiber, 0.10% cluster, and 1.00% ferric metal ion nanofiber. However, this peak could also be affected by PAA C=O stretching.

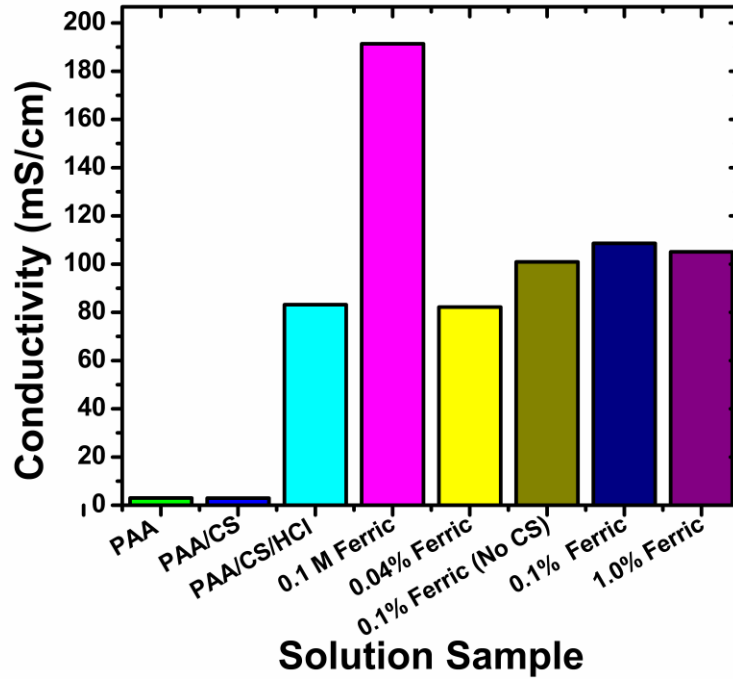


Figure 18. Conductivity of PAA:CS nanofiber and pre-fabrication component solutions. A clear pattern is not evident in ferric-containing pre-electrospinning solutions. Comparison of conductivity between PAA:CS and ferric-mixed solutions reveals a major rise with metal ions and therefore should lead to thinner diameter nanofibers.

Ferric Metal Ion Concentration (%)	Average Diameter (nm)	Young's Modulus (kPa)
0	202	3.25
PAA only (no CS) No Fe ³⁺	195	2.27
0.04	284	1.02
0.10	156-584	0.09-16.51
0.10 (No CS)	248-351	0.67-2.5
1.00	366-397	0.27-0.37

Table 1. Application of SEM diameter measurements as well as persistence length (using *Persistence* and *Origin* software) in calculations to give estimations for Young's modulus. Young's modulus is in the kPa range for individual nanofibers in their hydrated state and show optimal calculated estimates at 0.10% ferric metal ion concentration.

CHAPTER FOUR: DISCUSSION

The polyelectrolyte complexation of polyacrylic acid with chitosan has been well studied for formation of hydrogels (Chen et al., 2006; Malhotra et al., 2016; Penchev et al., 2008; Y. Wang et al., 2017), revealing the necessity for further crosslinking to ensure the network can withstand variability in its environment. Electrostatic interactions of amine (CS) and carboxylate (PAA) functional groups create hydrogels (Bogdanova et al., 2017; Chavasit et al., 1988; H. Wang et al., 1997) but do not allow optimization for higher pH variations or mechanical stresses without further processing. Metal ions have been known to interact with polyelectrolyte complexes in hydrogels to create the necessary resilience against environmental fluctuations (Filippidi et al., 2017; Guibal, 2004; Thünemann et al., 2004; Zheng et al., 2016), but study of their effect on the mechanics of *individual* nanofibers for tunability have been lacking. Our results suggest that metal ions interact with polyelectrolyte complexes in a manner that can help optimize electrospun nanofiber mechanics prior to hydrogel swelling. We showed that increasing ferric metal ion concentrations do not affect the bending stiffness or PAA:CS nanofiber length in a linear manner, instead reaching an optimum effect at a metal ion concentration of 0.10%, where stiffness is highest and nanofiber lengths are shortest (at lower concentrations). Chitosan was also studied to see how it would affect the changes made by the ferric metal ions, revealing that lack of its presence made for longer nanofibers but did not change the optimal concentration of 0.10% Fe^{3+} on bending stiffness measurements. Further characterization of the system in our studies indicated that most of the interactions affecting the system were between the positive charges of the metal ions and negative carboxyl groups of the polyacrylic acid due to protonation of chitosan at the lower pH of the electrospinning solution, though further study into characteristic peak areas for CS is necessary to

verify its lack of interaction completely with PAA and the metal ions due to the peak deconvolution range we chose having both PAA and CS peaks potentially showing too close to each other.

Our work has verified that addition of the metal ions allows the crosslinking necessary to enhance properties of individual nanofibers. Previous studies reveal that ferric could successfully bind with both chitosan and polyacrylic acid (Baigorri et al., 2007; Bhatia & Ravi, 2000; Nie et al., 2016; Wei et al., 2013; Zhong et al., 2016), consistent with the ferric ion's effect on PAA nanofibers in this study. However, protonation of the chitosan due to low pH hinders its electrostatic interaction with PAA and could be detrimental to hydrogel mechanics. If no other form of crosslinking is applied to compensate the lack of interaction between chitosan and PAA, the complex will not be sustainable for medical applications in such an environment. This effect is counter-balanced in our work by the ferric metal ions which form strong crosslinks electrostatically with PAA (Yokoi & Nishi, 1989). Previous research with application of varying types of metal ions has shown that ferric ions of a high valency make good crosslinkers with PAA due to their size to charge ratio and higher valency (Malhotra et al., 2016). Even at the same valency, the smaller the ion the less the same charge must be spread over the ion. Therefore, even though Fe^{3+} has the same valence as a metal ion such as Ce^{3+} , the small ferric ion has stronger interactions overall with PAA. The lower valency of other ions also seen in the study from Malhotra et al. did not allow as strong of an interaction and instead created a shielding effect between chitosan and polyacrylic acid as the pH rose, making the polymer complex more prone to dissolution.

Still, our results suggest that a threshold needs to be overcome before optimal effect of the ferric metal ions can be obtained for bending stiffness. Protonation of PAA is still possible and

could be one factor hindering ferric interactions at lower pH in concert with hindrance from chitosan. Competition between the positive charges of the chitosan, protons, and Fe^{3+} could be creating a repulsion effect within the system as ferric is being added, leading to the delay in rise of bending stiffness until the 0.10% concentration. It could also be the steric effect of the chains of chitosan which are drawn to the carboxylate groups of PAA and make it more difficult for the much smaller, less concentrated metal ions to reach the anionic charges. It has been suggested that ferric ions form clusters to which the polyacrylic acid is drawn to even in lower pH solutions where protonation of the carboxyl groups usually occur as shown in our results, which could explain how even with competition from CS and protons the PAA and Fe^{3+} still manage to form complexes even at lower concentrations of metal ions (Calvo-Marzal et al., 2011; Yokoi & Nishi, 1989; Yokoi et al., 1993).

The pre-electrospinning solution creation at a lower pH affected chitosan through protonation that kept interaction between it and the other components to an arguably negligible level, making most of the effect a focus between PAA and ferric metal ions (Baigorri et al., 2007; Malhotra et al., 2016). However, our studies on nanofiber mechanics with and without CS in the system showed the effect of its presence to a rise in concentration to 0.10%, at which bending stiffness average measurements were similar. Without chitosan present it was difficult to keep the system from gelation due to the strong interactions of PAA and Fe^{3+} and therefore higher measurements were not acquired. Though CS could be protonated, the steric hindrance provided by its presence could be slowing down creation of electrostatic interactions between PAA and the metal ions. The initial rise and then fall of PAA:CS: Fe^{3+} nanofiber bending stiffness before reaching the highest effect value is mostly reliant on the presence of CS, seeing as comparison to nanofibers with only

PAA:Fe³⁺ revealed a steady climb in their bending stiffness values. This boost could be due to the electrostatic interactions created by the ferric ions with multiple chains to make up for the lack of chitosan in the complex, as well as lack of competition for interactions with PAA (Baigorri et al., 2007; Wei et al., 2013; Zhong et al., 2016). Since chitosan does not fully block ferric interaction with PAA, it could rather help reinforce nanofibers physically. Results from FTIR and AFM-IR reinforce this theory due to the lack of peaks for chitosan functional groups on initial study, though further characterization is required for verification. When compared to studies done on PAA interaction with metal ions without the presence of other crosslinkers (Jones et al., 1998; Romalucio et al., 2000; Yokoi et al., 1993), our results showed similar lack of CS presence with exception of the main peak at 1650 cm⁻¹ in deconvolutions, though there is need to look at a wider range of CS characteristic peaks.

Of special interest in our study of bond interactions with FTIR was the single peak that showed at 1591cm⁻¹ at a ferric concentration of 1.00%, indicating ferric metal ion bidentate bridging in which the two oxygen groups attached to one carboxyl carbon of PAA interact with a ferric metal molecule each. This result was verified via further results of AFM IR studies, in which peak deconvolution was done on various nanofiber concentrations. As shown in the FTIR of higher concentrations, the peak was not as accurate of a representation when compared with AFM-IR results. These also showed varying peak changes throughout the concentrations studied, which could be indication of how the crosslinks are shifting within the structure, even while acting as clusters. Migration of the metal ions is key in self-healing structures for medical applications since their electrostatic nature allows them to create new crosslinks in severed materials (Wei et al., 2013; Zheng et al., 2016). At 0.10% Fe³⁺ concentration in both length and bending stiffness it can

be noted that the nanofibers reach a saturation point in bending stiffness and length changes, though how PAA, Fe^{3+} , and chitosan interact at this concentration requires further study considering the peak results of deconvolution.

While various studies done for the mechanics of hydrogels using different methods yielded a wide range of Young's modulus measurements (6-100,000 kPa) (Gulyuz & Okay, 2013, 2014; Lichter et al., 2008), the knowledge of Young's modulus for *individual* PAA nanofibers is lacking. Single fiber studies have focused on several polymer nanofibers with application of AFM three-point bend testing over ridges on customized substrates (S.-H. Lee et al., 2005; Y. Li & Wan, 2017; Shin et al., 2006; E. P. S. Tan & Lim, 2004). However, no applications for Young's modulus calculation have been proposed in which bending stiffness and diameter measurements are applied for estimation without direct measurement via other instrumentation. Our work therefore offers a technique of polymer strength measurement in single nanofibers without requiring more complex, time-consuming methods.

Though our calculations of Young's modulus have a wide range, they are within reasonable bounds when compared to other polymer materials. For instance, Marklein et al.'s study on methacrylated hyaluronic acid hydrogels yielded Young's modulus measurements in the range of 1.5-12.4 kPa with successful human mesenchymal stem cell growth (Marklein et al., 2012). Gulyuz and Okay fabricated PAA hydrogels of 6-53 kPa (Gulyuz & Okay, 2013), also overlapping with our own measurements and indicating that our nanofibers show acceptable strength estimates even in their dry states. Though other studies focusing on single nanofibers reported Young's modulus in the MPa-GPa range, it should be noted that their methods required AFM application of the three-point bend test (Cuenot et al., 2004; Shin et al., 2006; E. P. S. Tan & Lim, 2004), and

indicate a measurement of a force applied to the nanofiber in a small area as opposed to the full nanofiber elasticity. Such methods also require more complex instrumentation and manipulation at the nano-scale for suspension of the nanofiber over a groove in a customized substrate. The AFM cantilever tip can then induce a deflection of the material but can only focus on study of one nanofiber at a time, making it a more time-consuming methodology. The range in our measurements could be due to moisture from the atmosphere affecting nanofibers or age of some of the samples measured, leading to breakdown. It is known that nanofibers have significantly higher Young's modulus measurements in relation to lower diameter measures, while their higher diameter counterparts closer resemble measurements of macro-scale Young's modulus of the same material (Cuenot et al., 2004). The PAA:CS fiber Young's modulus range therefore shows room for improvement of mechanical characteristics.

Solution conductivity is known to influence electrospinning greatly, determining whether a solution will create uniform or beaded nanofibers, or ribbons. Most importantly conductivity in the critical range of a polymer solution could create uniform, thinner-diameter nanofibers desired for their higher Young's modulus. Based on conductivity results acquired, PAA:CS nanofibers without metal ions should create nanofibers with higher diameters and lower Young's modulus when compared to electrospinning solutions with any concentration of ferric. Results showed that ferric solutions with or without CS all had much higher values of conductivity when compared to PAA or PAA:CS-only measurements, though a pattern was not easy to reveal due to how close in value the metal ion solutions all were. The method used also included the solution prior to electrospinning, which accounted for conductivity of the solvent and therefore was not focused solely on metal ion influence. Further study into the effect of conductivity would consequently

have to be explored on the final product for better indication of impact by the metal ions for better control of mechanical strength.

CHAPTER FIVE: CONCLUSION

In-depth study of the effect of metal ions on polyelectrolyte nanofibers is necessary to understand if the effects could be tunable in nanofiber materials. Biomedical applications stand to benefit due to the nanofiber hydrogel's natural ability to mimic extracellular matrix, allowing for better drug delivery vehicles, wound dressings, and tissue scaffolds via swelling of electrospun polyelectrolyte nanofibers. The main conclusion to be drawn of our study is the tunability offered by metal ions over polyelectrolyte mechanics at the individual nanofiber level. Other studies have involved atomic force microscopy bend tests to measure mechanical characteristics, but such methodology requires complex instrumentation and time-consuming setup. Our results reveal how application of a technique usually reserved for biopolymers could be applied in estimations of nanofiber mechanical changes. Nonetheless, further research is required into application of our technique in comparison with other well-established methods.

We have shown how metal ions can modulate polyelectrolyte nanofiber mechanics in a tunable manner. Further characterization will help develop a clearer pattern of the effect of metal ions through expanded conductivity characterization for adjusted electrospinning. Additionally, further development of AFM application will give insight into structural and mechanical strength for comparison of our techniques and study of bending stiffness of nanofibers at further concentrations will clarify metal ion interaction patterns. Optimization of nanofiber mechanics will also include addition of new components such as proteins, which are already biocompatible and could come with added control of characteristics of the hydrogel through folding and unfolding of the electrospun proteins. We expect to develop our nanofiber material with addition of fibrinogen to enhance intrinsic properties of the hydrogel in anchorage of the bulk material to a wound area and

aid encouragement of suitable proliferation of wound healing cells while offering potential control of the hydrogel through protein folding/unfolding. Experimentation on all these fronts will aid in the creation of a material which could be applied to different environments of the body in a tunable manner and with adaptable mechanical characteristics. Our work focused on study of individual nanofibers in hopes that optimization at that level will further enhance the mechanics of hydrogels whose characteristic changes via metal ions have been well established. We look forward to creating a better understanding of the polyelectrolyte interaction with metal ions in application of polyelectrolytes for biomedical applications.

REFERENCES

- Ahmed, E. M. (2015). Hydrogel: Preparation, characterization, and applications: A review. *Journal of Advanced Research*, 6(2), 105-121. doi:<https://doi.org/10.1016/j.jare.2013.07.006>
- Anderson, M. S. (2000). Infrared Spectroscopy with an Atomic Force Microscope. *Applied Spectroscopy*, 54(3), 349-352.
- Angamma, C. J., & Jayaram, S. H. (2016). Fundamentals of electrospinning and processing technologies. *Particulate Science and Technology*, 34(1), 72-82. doi:10.1080/02726351.2015.1043678
- Anjum, S., Gurave, P., Badiger, M. V., Torris, A., Tiwari, N., & Gupta, B. (2017). Design and development of trivalent aluminum ions induced self-healing polyacrylic acid novel hydrogels. *Polymer*, 126, 196-205. doi:<https://doi.org/10.1016/j.polymer.2017.08.045>
- Arinstein, A., Burman, M., Gendelman, O., & Zussman, E. (2007). Effect of supramolecular structure on polymer nanofibre elasticity. *Nature Nanotechnology*, 2(1), 59-62. doi:<http://dx.doi.org/10.1038/nnano.2006.172>
- Arinstein, A., & Zussman, E. (2011). Electrospun polymer nanofibers: Mechanical and thermodynamic perspectives. *Journal of Polymer Science Part B: Polymer Physics*, 49(10), 691-707. doi:10.1002/polb.22247
- Baigorri, R., García-Mina, J. M., & González-Gaitano, G. (2007). Supramolecular association induced by Fe (III) in low molecular weight sodium polyacrylate. *Colloids and Surfaces A: Physicochemical and Engineering Aspects*, 292(2), 212-216.
- Bhardwaj, N., & Kundu, S. C. (2010). Electrospinning: A fascinating fiber fabrication technique. *Biotechnology Advances*, 28(3), 325-347. doi:<https://doi.org/10.1016/j.biotechadv.2010.01.004>
- Bhatia, S. C., & Ravi, N. (2000). A magnetic study of an Fe- chitosan complex and its relevance to other biomolecules. *Biomacromolecules*, 1(3), 413-417.
- Bogdanova, O. I., Polyakov, D. K., Streltsov, D. R., Kulebyakina, A. I., Orekhov, A. S., Vasiliev, A. L., . . . Chvalun, S. N. (2017). Fabrication and mechanical properties of composite based on beta-chitin and polyacrylic acid. *Carbohydr Polym*, 157, 1496-1502. doi:10.1016/j.carbpol.2016.11.032
- Calvo-Marzal, P., Delaney, M. P., Auletta, J. T., Pan, T., Perri, N. M., Weiland, L. M., . . . Meyer, T. Y. (2011). Manipulating mechanical properties with electricity: electroplastic elastomer hydrogels. *ACS Macro Letters*, 1(1), 204-208.
- Camposo, A., Greenfeld, I., Tantussi, F., Pagliara, S., Moffa, M., Fuso, F., . . . Pisignano, D. (2013). Local Mechanical Properties of Electrospun Fibers Correlate to Their Internal Nanostructure. *Nano Letters*, 13(11), 5056-5062. doi:10.1021/nl4033439
- Chavasit, V., Kienzle-Sterzer, C., & Antonio Torres, J. (1988). Formation and characterization of an insoluble polyelectrolyte complex: chitosan-polyacrylic acid. *Polymer Bulletin*, 19(3), 223-230.
- Chen, C. Y., Wang, J. W., & Hon, M. H. (2006). Polyion Complex Nanofibrous Structure Formed by Self Assembly of Chitosan and Poly (acrylic acid). *Macromolecular Materials and Engineering*, 291(2), 123-127.

- Coates, J. (2006). Interpretation of Infrared Spectra, A Practical Approach. In *Encyclopedia of Analytical Chemistry*: John Wiley & Sons, Ltd.
- Cuenot, S., Frétiigny, C., Demoustier-Champagne, S., & Nysten, B. (2004). Surface tension effect on the mechanical properties of nanomaterials measured by atomic force microscopy. *Physical Review B*, *69*(16), 165410.
- Dazzi, A., Prater, C. B., Hu, Q., Chase, D. B., Rabolt, J. F., & Marcott, C. (2012). AFM–IR: Combining Atomic Force Microscopy and Infrared Spectroscopy for Nanoscale Chemical Characterization. *Applied Spectroscopy*, *66*(12), 1365-1384. doi:10.1366/12-06804
- Dehghani, E. S., Naik, V. V., Mandal, J., Spencer, N. D., & Benetti, E. M. (2017). Physical Networks of Metal-Ion-Containing Polymer Brushes Show Fully Tunable Swelling, Nanomechanical and Nanotribological Properties. *Macromolecules*, *50*(6), 2495-2503. doi:10.1021/acs.macromol.6b02673
- Desai, K., Kit, K., Li, J., & Zivanovic, S. (2008). Morphological and Surface Properties of Electrospun Chitosan Nanofibers. *Biomacromolecules*, *9*(3), 1000-1006. doi:10.1021/bm701017z
- Dong, J., Ozaki, Y., & Nakashima, K. (1997). Infrared, Raman, and Near-Infrared Spectroscopic Evidence for the Coexistence of Various Hydrogen-Bond Forms in Poly(acrylic acid). *Macromolecules*, *30*(4), 1111-1117. doi:10.1021/ma960693x
- Engler, A. J., Sen, S., Sweeney, H. L., & Discher, D. E. (2006). Matrix elasticity directs stem cell lineage specification. *Cell*, *126*(4), 677-689.
- Filippidi, E., Cristiani, T. R., Eisenbach, C. D., Waite, J. H., Israelachvili, J. N., Ahn, B. K., & Valentine, M. T. (2017). Toughening elastomers using mussel-inspired iron-catechol complexes. *Science*, *358*(6362), 502.
- Francis Michael, P., Moghaddam-White Yas, M., Sachs Patrick, C., Beckman Matthew, J., Chen Stephen, M., Bowlin Gary, L., . . . Holt Shawn, E. (2016). Modeling early stage bone regeneration with biomimetic electrospun fibrinogen nanofibers and adipose-derived mesenchymal stem cells. In *Electrospinning* (Vol. 1, pp. 10).
- Geckil, H., Xu, F., Zhang, X., Moon, S., & Demirci, U. (2010). Engineering hydrogels as extracellular matrix mimics. *Nanomedicine (London, England)*, *5*(3), 469-484. doi:10.2217/nmm.10.12
- Graham, J. S., McCullough, B. R., Kang, H., Elam, W. A., Cao, W., & Enrique, M. (2014). Multi-platform compatible software for analysis of polymer bending mechanics. *PloS one*, *9*(4), e94766.
- Guibal, E. (2004). Interactions of metal ions with chitosan-based sorbents: a review. *Separation and Purification Technology*, *38*(1), 43-74. doi:https://doi.org/10.1016/j.seppur.2003.10.004
- Guibal, E., Vincent, T., & Navarro, R. (2014). Metal ion biosorption on chitosan for the synthesis of advanced materials. *Journal of Materials Science*, *49*(16), 5505-5518. doi:10.1007/s10853-014-8301-5
- Gulyuz, U., & Okay, O. (2013). Self-healing polyacrylic acid hydrogels. *Soft Matter*, *9*(43), 10287-10293.
- Gulyuz, U., & Okay, O. (2014). Self-healing poly (acrylic acid) hydrogels with shape memory behavior of high mechanical strength. *Macromolecules*, *47*(19), 6889-6899.
- Haider, A., Haider, S., & Kang, I.-K. (2015). A comprehensive review summarizing the effect of electrospinning parameters and potential applications of nanofibers in biomedical and

- biotechnology. *Arabian Journal of Chemistry*.
doi:<https://doi.org/10.1016/j.arabjc.2015.11.015>
- Hammiche, A., Pollock, H. M., Reading, M., Claybourn, M., Turner, P. H., & Jewkes, K. (1999). Photothermal FT-IR Spectroscopy: A Step Towards FT-IR Microscopy at a Resolution Better Than the Diffraction Limit. *Applied Spectroscopy*, *53*(7), 810-815.
- Haraguchi, K., Uyama, K., & Tanimoto, H. (2011). Self-healing in Nanocomposite Hydrogels. *Macromolecular Rapid Communications*, *32*(16), 1253-1258. doi:10.1002/marc.201100248
- Hoerter, M., Oprea, A., Bârsan, N., & Weimar, U. (2008). Chemical interaction of gaseous ammonia and water vapour with polyacrylic acid layers. *Sensors and Actuators B: Chemical*, *134*(2), 743-749. doi:<https://doi.org/10.1016/j.snb.2008.06.026>
- Hoffman, A. S. (2012). Hydrogels for biomedical applications. *Advanced Drug Delivery Reviews*, *64*, 18-23. doi:<https://doi.org/10.1016/j.addr.2012.09.010>
- Howard, J. (2001). *Mechanics of motor proteins and the cytoskeleton*: Sunderland, Mass. : Sinauer Associates, Publishers, c2001.
- Jian-Gang Guo and Ya-Pu, Z. (2007). The size-dependent bending elastic properties of nanobeams with surface effects. *Nanotechnology*, *18*(29), 295701.
- Jones, F., Farrow, J. B., & van Bronswijk, W. (1998). An Infrared Study of a Polyacrylate Flocculant Adsorbed on Hematite. *Langmuir*, *14*(22), 6512-6517. doi:10.1021/la971126l
- Kelly, P. (2013). Solid mechanics part I: An introduction to solid mechanics. *Solid mechanics lecture notes*.
- Kim, T. H., Ahn, J. S., Choi, H. K., Choi, Y. J., & Cho, C. S. (2007). A Novel Mucoadhesive Polymer Film Composed of Carbopol, Poloxamer and Hydroxypropylmethylcellulose. *Archives of Pharmacal Research*, *30*(3), 381-386. doi:10.1007/BF02977622
- Kirwan, L. J., Fawell, P. D., & van Bronswijk, W. (2003). In Situ FTIR-ATR Examination of Poly(acrylic acid) Adsorbed onto Hematite at Low pH. *Langmuir*, *19*(14), 5802-5807. doi:10.1021/la027012d
- Lee, J. W., Kim, S. Y., Kim, S. S., Lee, Y. M., Lee, K. H., & Kim, S. J. (1999). Synthesis and characteristics of interpenetrating polymer network hydrogel composed of chitosan and poly (acrylic acid). *Journal of Applied Polymer Science*, *73*(1), 113-120.
- Lee, S.-H., Tekmen, C., & Sigmund, W. M. (2005). Three-point bending of electrospun TiO₂ nanofibers. *Materials Science and Engineering: A*, *398*(1), 77-81. doi:<https://doi.org/10.1016/j.msea.2005.03.014>
- Li, D., & Xia, Y. (2004). Electrospinning of nanofibers: reinventing the wheel? *Advanced materials*, *16*(14), 1151-1170.
- Li, L., & Hsieh, Y.-L. (2005). Ultra-fine polyelectrolyte fibers from electrospinning of poly (acrylic acid). *Polymer*, *46*(14), 5133-5139.
- Li, Y., & Wan, W. (2017). Exploring Polymer Nanofiber Mechanics: A review of the methods for determining their properties. *IEEE Nanotechnology Magazine*, *11*(3), 16-28. doi:10.1109/MNANO.2017.2708819
- Lichter, J. A., Thompson, M. T., Delgadillo, M., Nishikawa, T., Rubner, M. F., & Van Vliet, K. J. (2008). Substrata mechanical stiffness can regulate adhesion of viable bacteria. *Biomacromolecules*, *9*(6), 1571-1578.
- Maitra, J., & Shukla, V. K. (2014). Cross-linking in hydrogels-a review. *American Journal of Polymer Science*, *4*(2), 25-31.

- Malhotra, A., Bera, T., & Zhai, L. (2016). Bioinspired Metal Ion Coordinated Polyelectrolyte Fibrous Nanoreactors. *Advanced Materials Interfaces*, 3(22), n/a.
- Marklein, R. A., Soranno, D. E., & Burdick, J. A. (2012). Magnitude and presentation of mechanical signals influence adult stem cell behavior in 3-dimensional macroporous hydrogels. *Soft Matter*, 8(31), 8113-8120. doi:10.1039/C2SM25501D
- McCullough, B. R., Blanchoin, L., Martiel, J.-L., & Enrique, M. (2008). Cofilin increases the bending flexibility of actin filaments: implications for severing and cell mechanics. *Journal of molecular biology*, 381(3), 550-558.
- Meng, L., Klinkajon, W., Harkin, S., Supaphol, P., & Wnek, G. E. (2015). Electrospun crosslinked poly (acrylic acid) fiber constructs: towards a synthetic model of the cortical layer of nerve. *Polymer International*, 64(1), 42-48.
- Miyamoto, T., & Shibayama, K. (1973). Free-volume model for ionic conductivity in polymers. *Journal of Applied Physics*, 44(12), 5372-5376. doi:10.1063/1.1662158
- Nakielski, P., Pawłowska, S., Pierini, F., Liwińska, W., Hejduk, P., Zembrzycki, K., . . . Kowalewski, T. A. (2015). Hydrogel Nanofilaments via Core-Shell Electrospinning. *PLOS ONE*, 10(6), e0129816. doi:10.1371/journal.pone.0129816
- Nam, S. Y., & Lee, Y. M. (1997). Pervaporation and properties of chitosan-poly (acrylic acid) complex membranes. *Journal of membrane science*, 135(2), 161-171.
- Nie, J., Wang, Z., & Hu, Q. (2016). Chitosan Hydrogel Structure Modulated by Metal Ions. *Scientific reports*, 6, 36005.
- Oatley, K. C. A. S. a. C. W. (1955). The scanning electron microscope and its fields of application. *British Journal of Applied Physics*, 6(11), 391.
- Omidian, H., & Park, K. (2010). Introduction to hydrogels. In *Biomedical applications of hydrogels handbook* (pp. 1-16): Springer.
- Ostroha, J., Pong, M., Lowman, A., & Dan, N. (2004). Controlling the collapse/swelling transition in charged hydrogels. *Biomaterials*, 25(18), 4345-4353. doi:https://doi.org/10.1016/j.biomaterials.2003.11.019
- Ott, A., Magnasco, M., Simon, A., & Libchaber, A. (1993). Measurement of the persistence length of polymerized actin using fluorescence microscopy. *Physical Review E*, 48(3), R1642-R1645.
- Penchev, H., Paneva, D., Manolova, N., & Rashkov, I. (2008). Novel Electrospun Nanofibers Composed of Polyelectrolyte Complexes. *Macromolecular Rapid Communications*, 29(8), 677-681. doi:10.1002/marc.200700844
- Qiu, Y., & Park, K. (2001). Environment-sensitive hydrogels for drug delivery. *Advanced Drug Delivery Reviews*, 53(3), 321-339. doi:https://doi.org/10.1016/S0169-409X(01)00203-4
- Reneker, D. H., & Yarin, A. L. (2008). Electrospinning jets and polymer nanofibers. *Polymer*, 49(10), 2387-2425.
- Roma-Luciw, R., Sarraf, L., & Morcellet, M. (2000). Concentration effects during the formation of poly (acrylic acid)-metal complexes in aqueous solutions. *Polymer Bulletin*, 45(4), 411-418. doi:10.1007/s002890070015
- Seiler, H. (1983). Secondary electron emission in the scanning electron microscope. *Journal of Applied Physics*, 54(11), R1-R18. doi:10.1063/1.332840
- Shetzline, J. A., & Creager, S. E. (2014). Quantifying Electronic and Ionic Conductivity Contributions in Carbon/Polyelectrolyte Composite Thin Films. *Journal of The Electrochemical Society*, 161(14), H917-H923.

- Shin, M. K., Kim, S. I., Kim, S. J., Kim, S.-K., & Lee, H. (2006). Reinforcement of polymeric nanofibers by ferritin nanoparticles. *Applied Physics Letters*, 88(19), 193901. doi:10.1063/1.2200469
- Singh, T., & Singhal, R. (2012). Poly(acrylic acid/acrylamide/sodium humate) superabsorbent hydrogels for metal ion/dye adsorption: Effect of sodium humate concentration. *Journal of Applied Polymer Science*, 125(2), 1267-1283. doi:10.1002/app.35435
- Smitha, B., Sridhar, S., & Khan, A. A. (2004). Polyelectrolyte Complexes of Chitosan and Poly(acrylic acid) As Proton Exchange Membranes for Fuel Cells. *Macromolecules*, 37(6), 2233-2239. doi:10.1021/ma0355913
- Smyth, M., Fournier, C., Driemeier, C., Picart, C., Foster, E. J., & Bras, J. (2017). Tunable Structural and Mechanical Properties of Cellulose Nanofiber Substrates in Aqueous Conditions for Stem Cell Culture. *Biomacromolecules*, 18(7), 2034-2044. doi:10.1021/acs.biomac.7b00209
- Stachowiak, A. N., Bershteyn, A., Tzatzalos, E., & Irvine, D. J. (2005). Bioactive hydrogels with an ordered cellular structure combine interconnected macroporosity and robust mechanical properties. *Advanced Materials*, 17(4), 399-403.
- Su, P., Wang, C., Yang, X., Chen, X., Gao, C., Feng, X.-X., . . . Gou, Z. (2011). Electrospinning of chitosan nanofibers: The favorable effect of metal ions. *Carbohydrate Polymers*, 84(1), 239-246. doi:https://doi.org/10.1016/j.carbpol.2010.11.031
- Takei, T., Nakahara, H., Ijima, H., & Kawakami, K. (2012). Synthesis of a chitosan derivative soluble at neutral pH and gellable by freeze–thawing, and its application in wound care. *Acta Biomaterialia*, 8(2), 686-693. doi:https://doi.org/10.1016/j.actbio.2011.10.005
- Tan, E. P. S., & Lim, C. T. (2004). Physical properties of a single polymeric nanofiber. *Applied Physics Letters*, 84(9), 1603-1605. doi:10.1063/1.1651643
- Tan, S. H., Inai, R., Kotaki, M., & Ramakrishna, S. (2005). Systematic parameter study for ultra-fine fiber fabrication via electrospinning process. *Polymer*, 46(16), 6128-6134. doi:https://doi.org/10.1016/j.polymer.2005.05.068
- Thünemann, A. F., Müller, M., Dautzenberg, H., Joanny, J.-F., & Löwen, H. (2004). Polyelectrolyte Complexes. In M. Schmidt (Ed.), *Polyelectrolytes with Defined Molecular Architecture II* (pp. 113-171). Berlin, Heidelberg: Springer Berlin Heidelberg.
- Tibbitt, M. W., & Anseth, K. S. (2009). Hydrogels as Extracellular Matrix Mimics for 3D Cell Culture. *Biotechnology and bioengineering*, 103(4), 655-663. doi:10.1002/bit.22361
- Todica, M., Stefan, R., Pop, C., & Olar, L. (2015). IR and Raman Investigation of Some Poly(acrylic) Acid Gels in Aqueous and Neutralized State. *Acta Physica Polonica A*, 128(1), 128-135. doi:10.12693/APhysPolA.128.128
- Wang, H., Li, W., Lu, Y., & Wang, Z. (1997). Studies on chitosan and poly(acrylic acid) interpolymer complex. I. Preparation, structure, pH-sensitivity, and salt sensitivity of complex-forming poly(acrylic acid): Chitosan semi-interpenetrating polymer network. *Journal of Applied Polymer Science*, 65(8), 1445-1450. doi:10.1002/(SICI)1097-4628(19970822)65:8<1445::AID-APP1>3.0.CO;2-G
- Wang, J. H. C., & Thampatty, B. P. (2006). An Introductory Review of Cell Mechanobiology. *Biomechanics and Modeling in Mechanobiology*, 5(1), 1-16. doi:10.1007/s10237-005-0012-z

- Wang, Y., Wang, J., Yuan, Z., Han, H., Li, T., Li, L., & Guo, X. (2017). Chitosan cross-linked poly(acrylic acid) hydrogels: Drug release control and mechanism. *Colloids and Surfaces B: Biointerfaces*, 152, 252-259. doi:http://dx.doi.org/10.1016/j.colsurfb.2017.01.008
- Wei, Z., He, J., Liang, T., Oh, H., Athas, J., Tong, Z., . . . Nie, Z. (2013). Autonomous self-healing of poly (acrylic acid) hydrogels induced by the migration of ferric ions. *Polymer Chemistry*, 4(17), 4601-4605.
- Yokoi, H., & Nishi, H. (1989). Interaction Mode Between Poly(acrylic acid) and Fe³⁺ Ions. Gelation Mechanism of the System. *Chemistry Letters*, 18(10), 1765-1768. doi:10.1246/cl.1989.1765
- Yokoi, H., Nomoto, E., & Ikoma, S. (1993). Reversible formation of iron(III) ion clusters in the poly(acrylic acid)-Fe³⁺ complex gel with changes in the water content. *Journal of Materials Chemistry*, 3(4), 389-392. doi:10.1039/JM9930300389
- Zheng, S. Y., Ding, H., Qian, J., Yin, J., Wu, Z. L., Song, Y., & Zheng, Q. (2016). Metal-Coordination Complexes Mediated Physical Hydrogels with High Toughness, Stick-Slip Tearing Behavior, and Good Processability. *Macromolecules*, 49(24), 9637-9646. doi:10.1021/acs.macromol.6b02150
- Zhong, M., Liu, Y.-T., Liu, X.-Y., Shi, F.-K., Zhang, L.-Q., Zhu, M.-F., & Xie, X.-M. (2016). Dually cross-linked single network poly (acrylic acid) hydrogels with superior mechanical properties and water absorbency. *Soft matter*, 12(24), 5420-5428.
- Zhong, M., Liu, Y.-T., & Xie, X.-M. (2015a). Self-healable, super tough graphene oxide-poly (acrylic acid) nanocomposite hydrogels facilitated by dual cross-linking effects through dynamic ionic interactions. *Journal of Materials Chemistry B*, 3(19), 4001-4008.
- Zhong, M., Liu, Y.-T., & Xie, X.-M. (2015b). Self-healable, super tough graphene oxide-poly (acrylic acid) nanocomposite hydrogels facilitated by dual cross-linking effects through dynamic ionic interactions. *Journal of Materials Chemistry B*, 3(19), 4001-4008.
- Zhu, Y., Xuan, H., Ren, J., & Ge, L. (2015). Self-healing multilayer polyelectrolyte composite film with chitosan and poly (acrylic acid). *Soft Matter*, 11(43), 8452-8459.